Aalborg Universitet

AALBORG UNIVERSITY
DENMARK

UPWARDS Deliverable D5.4

Report and data on the effect of fatigue loading history on damage development

Mosbjerg Jensen, Simon; Carreras, Laura; Lindgaard, Esben; Bak, Brian Lau Verndal; Krumenacker, Nicolas; Lequesne, Cedric

Publication date:
2021

Document Version
Publisher's PDF, also known as Version of record

Link to publication from Aalborg University

Citation for published version (APA):
Mosbjerg Jensen, S., Carreras, L., Lindgaard, E., Bak, B. L. V., Krumenacker, N., & Lequesne, C. (2021). *UPWARDS Deliverable D5.4: Report and data on the effect of fatigue loading history on damage development*.

General rights
Copyright and moral rights for the publications made accessible in the public portal are retained by the authors and/or other copyright owners and it is a condition of accessing publications that users recognise and abide by the legal requirements associated with these rights.

- Users may download and print one copy of any publication from the public portal for the purpose of private study or research.
- You may not further distribute the material or use it for any profit-making activity or commercial gain
- You may freely distribute the URL identifying the publication in the public portal -

Take down policy
If you believe that this document breaches copyright please contact us at vbn@aub.aau.dk providing details, and we will remove access to the work immediately and investigate your claim.

Downloaded from vbn.aau.dk on: May 14, 2024

Ref. Ares(2022)3172045 - 22/04/2022

Grant Agreement N°763990

UPWARDS

Deliverable D5.4

Report and data on the effect of fatigue loading history on damage development

WP	5	Material failure models
Task	5.4	Effect of fatigue loading history on damage development (inter- and intra-laminar)

Dissemination level[1]	PU
Nature[2]	R

Due delivery date	30/07/2021 (30/10/2021)
Actual delivery date	XX/XX/XXXX

Lead beneficiary	**Aalborg University**
Contributing beneficiaries	SAMTECH SA, SINTEF, SGRE

Document Version	Date	Author	Comments[3]
4	30/03/2022	Simon Mosbjerg Jensen (AAU), Laura Carreras (AAU), Esben Lindgaard (AAU), Brian Bak (AAU), Nicolas Krumenacker (SINTEF), Cédric Lequesne (SAMTECH)	Creation

[1] Dissemination level: **PU** = Public, **PP** = Restricted to other programme participants (including the JU), **RE** = Restricted to a group specified by the consortium (including the JU), **CO** = Confidential, only for members of the consortium (including the JU)

[2] Nature of the deliverable: **R** = Report, **P** = Prototype, **D** = Demonstrator, **O** = Other

[3] Creation, modification, final version for evaluation, revised version following evaluation, final

Deliverable abstract

Fracture in laminated composites is typically caused by inter-laminar damage, such as delamination, promoted by or coexisting with intra-laminar damage, like matrix-cracking and fibre failure. During operation of composite structures, these damage mechanisms initiate and propagate under variable amplitude loading conditions that are very different from the constant amplitude loading conditions applied to test specimens in laboratories to characterise fatigue properties of the material. The work in Task 5.4 focuses on the effect of variable amplitude loading on the damage evolution in fiber reinforced polymer laminated composites. An experimental test campaign investigates fatigue-driven delamination under multi-level block loading, and a new crack growth rate model is proposed. The crack growth rate model is included in a finite element formulation as an extension of the inter-laminar fatigue damage method from Task 5.1. The method has been implemented in the Simcenter Samcef software. The simulated results from the Simcenter Samcef solver show a significant improvement in the delamination growth prediction in comparison to the conventional non-interaction crack growth rate model. Another experimental campaign investigates intra-laminar damage under two-level block loading. The experiments subject specimens to flexural fatigue loading using a simplified test configuration that can be readily implemented by most any research group with access to a universal fatigue testing machine. The simplified experimental setup used in this work was suitable to investigate the load history effects on intralaminar damage evolution.

Deliverable Review

	Reviewer #1: /Coordinator			**Reviewer #2:**		
	Answer	**Comments**	**Type***	**Answer**	**Comments**	**Type***
1. Is the deliverable in accordance with						
(i) The Description of Work?	☒ Yes ☐ No		☐ M ☐ m ☐ a	☐ Yes ☐ No		☐ M ☐ m ☐ a
(ii) The international State of the Art?	☐ Yes ☐ No	*Not applicable for this deliverable*	☐ M ☐ m ☐ a	☐ Yes ☐ No	*Not applicable for this deliverable*	☐ M ☐ m ☐ a
2. Is the quality of the deliverable in a status						
(i) That allows it to be sent to European Commission?	☒ Yes ☐ No		☐ M ☐ m ☐ a	☐ Yes ☐ No		☐ M ☐ m ☐ a
(ii) That needs improvement of the writing by the originator of the deliverable?	☐ Yes ☒ No		☐ M ☐ m ☐ a	☐ Yes ☐ No		☐ M ☐ m ☐ a
(iii) That needs further work by the Partners responsible for the deliverable?	☐ Yes ☒ No		☐ M ☐ m ☐ a	☐ Yes ☐ No		☐ M ☐ m ☐ a

* Type of comments: M = Major comment; m = minor comment; a = advice

Table of Contents

1. Introduction

Failure in laminated composites is usually caused by inter-laminar fractures, such as delamination or adhesive joint debonding, promoted by or coexisting with intra-laminar damage mechanisms, like matrix cracking and fibre failure (see Figure 1-1).

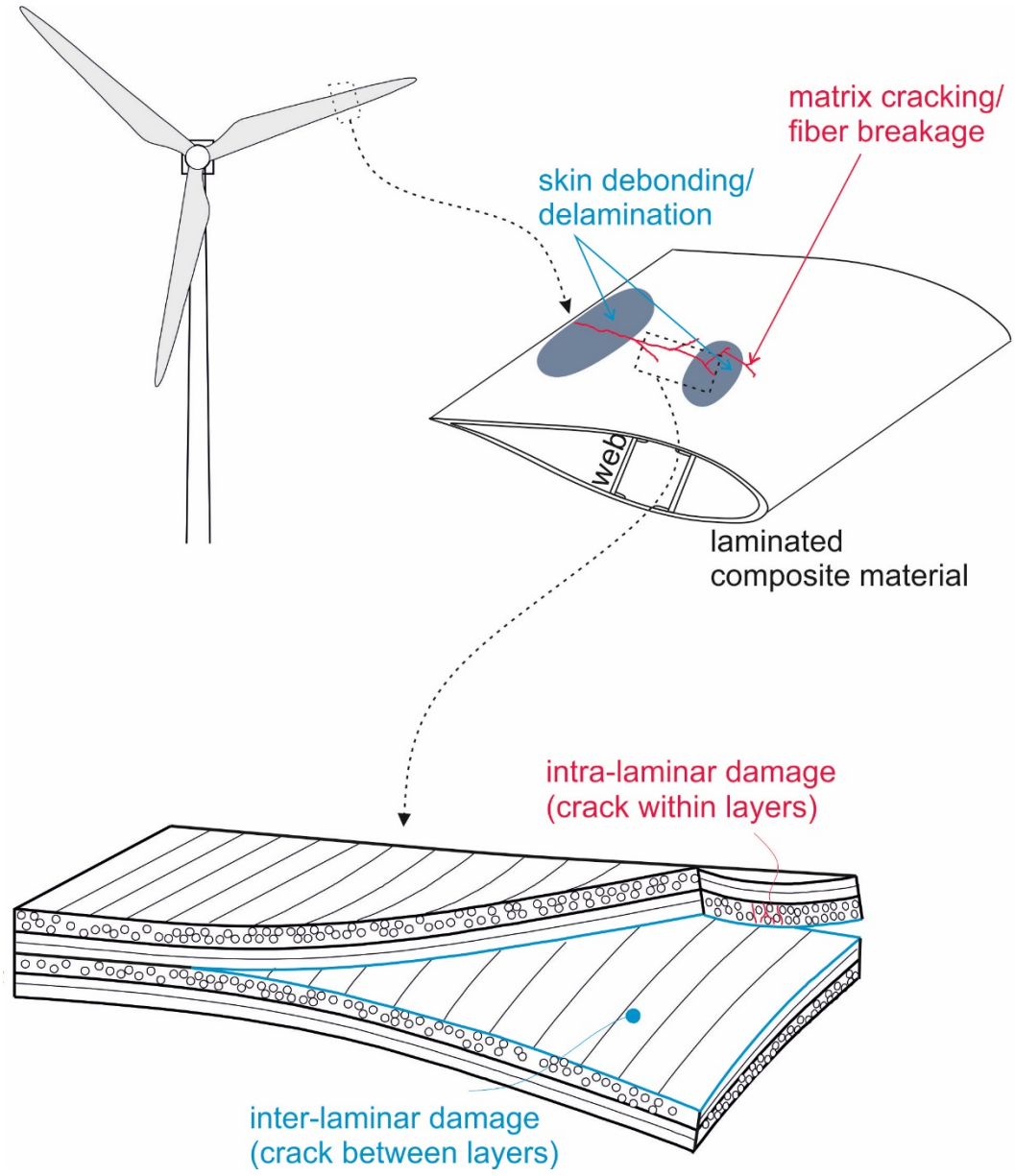

Figure 1-1. Inter-laminar and intra-laminar damage in wind turbine blades made of a laminated composite material.

Fatigue failure prediction is crucial for a safe and efficient design, an accurate assessment of the service life of composite structures and as a planning tool for maintenance actions. State-of-the-art material damage models are not capable to model the interaction between different failure mechanisms, such as inter- and intra-laminar damage cf. Fig. 1-1, and the complexity of realistic loading spectra of varying amplitude and frequency, which composite structures experience during operation. The objectives of WP5 are the development of (i) progressive material damage models for both inter- and intra-laminar fracture and (ii) simulation tools for static and fatigue-driven damage development in laminated composite wind turbine blades to evaluate the structural performance and integrity.

First, independent inter- and intra-laminar fatigue damage models are developed in Task 5.1 and Task 5.2, respectively. Then, a unified numerical framework is implemented in the Simcenter Samcef

solver, including interaction between both models in Task 5.3. Then, the effect of fatigue loading history on damage development is studied and incorporated in the numerical tool in Task 5.4. Finally, the method is validated against experimental testing on a wind turbine (WT) blade substructure in Task 5.5. The described workflow is illustrated in Figure 1-2.

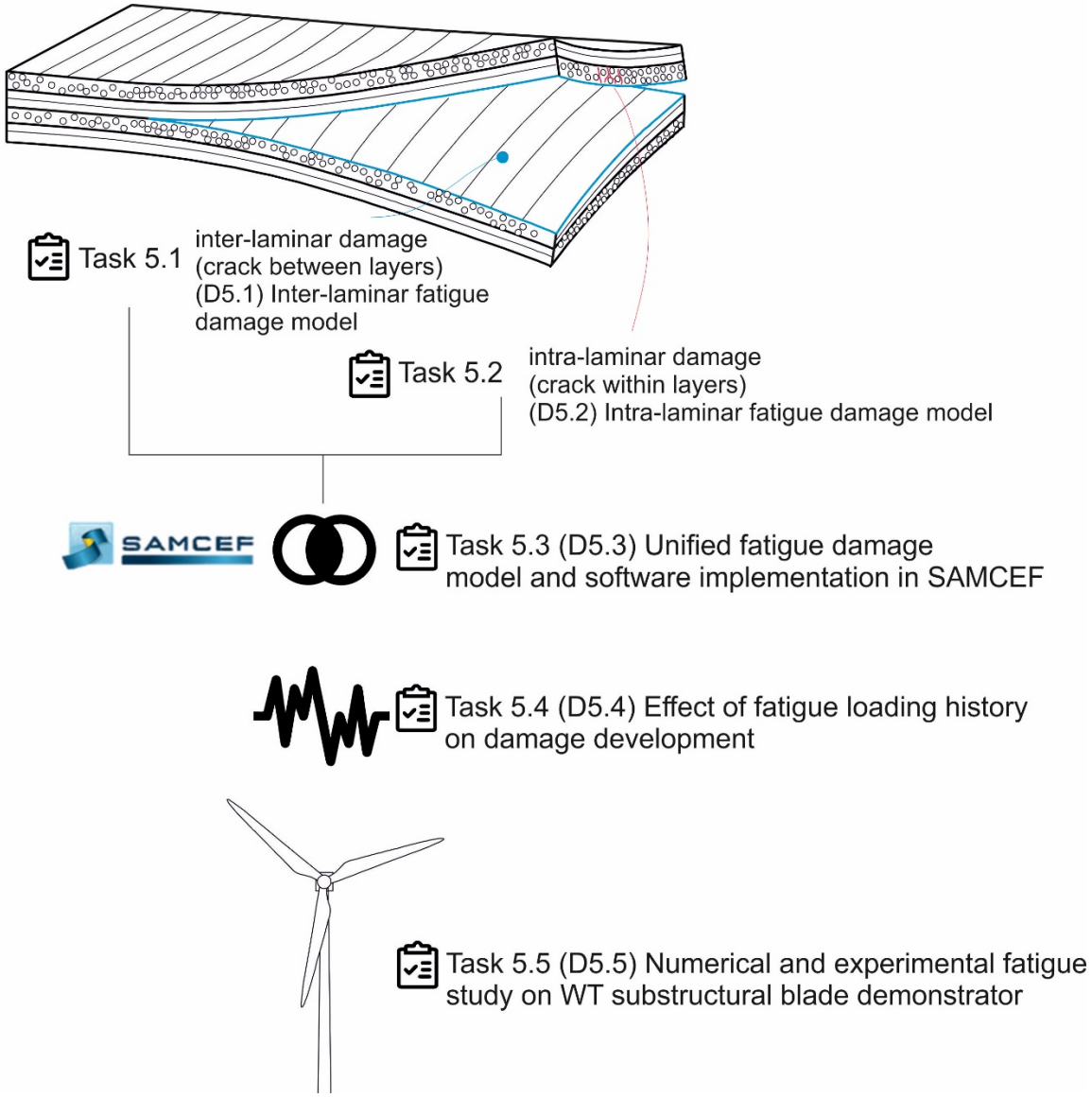

Figure 1-2. Overview of tasks in work package WP5.

This document describes the work carried out in Task 5.4 about physically understanding how damage development is influenced by the fatigue loading history. AAU has performed an experimental campaign focusing first on inter-laminar damage using an automatic high-resolution optical crack tracking system to capture transition effects in damage development due to changes in loading amplitude. Loading history effects and error with existing fatigue models have been quantified. AAU has developed a model of the transition effects and experimentally validated the effect of loading history on damage development. AAU has extended the inter-laminar fatigue damage finite element method from Task 5.1 and SAMTECH has implemented the method in the Simcenter Samcef software and validated it numerically. SINTEF has conducted an experimental study of the evolution of intralaminar damage under flexural fatigue loading. SGRE has provided all coupon test specimens needed to perform the testing. The workflow of Task 5.4 is illustrated in Fig. 1-3.

.

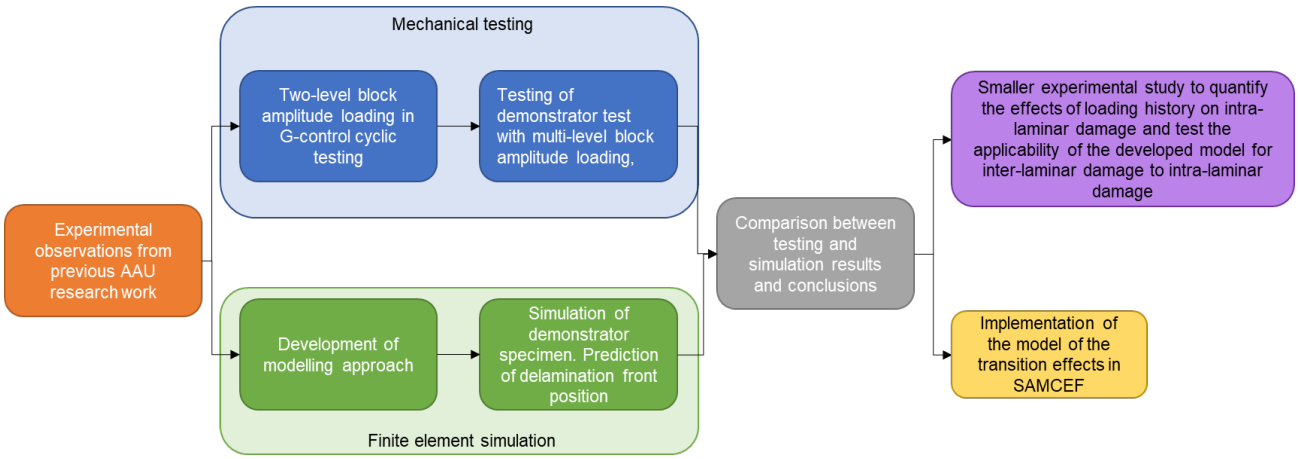

Figure 1-3. Workflow in Task 5.4.

This deliverable D5.4 is structured as follows: Section 1 provides the background and motivation of this study. Section 2 presents an experimental campaign on fatigue-driven delamination under two- and multi-level block loading and proposes a new crack growth rate model to include load interaction effects in delamination growth predictions. Section 3 focus on implementation of the new crack growth rate model in a finite element formulation, as an extension of the inter-laminar fatigue damage finite element method from Task 5.1. Section 4 describes the implementation of the inter-laminar damage method in the Simcenter Samcef software and numerical validation studies. Section 5 presents an experimental study on the effect of load history on the evolution of intralaminar damage under flexural fatigue loading. Section 6 concludes the work.

1.1. Background

There is a vast gap between the constant amplitude (CA) loading conditions, which are applied to test specimens in the laboratory for characterization of fatigue properties, and the load spectra that composite structures experience in-service, also known as real load spectra. A real load spectrum comprises variable amplitudes and mean loads of irregular sequence and with frequent load amplitude changes [1, 2]. Variable amplitude (VA) fatigue experiments of laminated fiber reinforced polymers (FRP) prove that these materials are highly sensitive to load interaction effects [2], i.e. the phenomenon that a damage growth increment in a given load cycle depends on the history of load cycles. The experimental approaches to VA fatigue of FRP laminates use one of the following three types of loading spectra [3]: Block loading spectra, standardized loading spectra, and stochastic loading spectra. Block loading tests consist of two or more CA loading blocks with different amplitude and mean values. The complexity of the block loading tests is typically low and limited to two to four amplitude and mean values [3]. The block loading tests yield a stepping-stone between CA loading and VA in-service loading, however, the tests are seldom representative of in-service loading. Nevertheless, certain combinations of load events are known to cause load interaction effects, and the block loading tests are often applied to improve the understanding of such. For example, the load sequence effect, which refers to a difference in fatigue life of composite components under low-high and high-low load sequences, has received a lot of attention in the literature [4, 5, 6, 7, 8, 9]. However, the experimental works in the literature use different materials, laminate architectures, and loading conditions, which gives no general consensus as to which load sequence causes more damage [10]. The cycle-mix effect is another prominent load interaction effect. The cycle-mix effect was originally described in [2] where it is observed that the residual strength and fatigue life of laminated composites decrease more rapidly when the load sequence is repeatedly changed after only few load cycles, i.e. frequent load amplitude changes causes an increased damage. The cycle-mix effect is afterwards studied in several modelling approaches and experiments, which is often

conducted using two-level block loading with repeated high and low load blocks. Example of studies on the cycle-mix effect include the residual strength- [11, 12] and residual stiffness-based modelling approaches [10], fatigue life predictions with a new cycle mix counting algorithm [13], multi-level block loading experiments with acoustic emission for damage monitoring [14], VA testing and fatigue-life prediction of adhesively bonded joints [15, 8]. Among the load sequence effect and the cycle-mix effect, the latter is considered as the dominant effect for most practical loadings due to the frequent changes in load amplitude level [2, 11, 12]. Next to the block loading experiments, the majority of available experimental data on VA spectrum loading of FRP laminates have been performed using standardized load spectra [3, 13, 16, 17, 18, 19, 20, 2, 12]. The standardized load spectra are load spectra that have been derived based on samples of recorded load-time histories of structures in-service and should carry the typical features of the load environments of a certain class of structures. Examples of standardized load spectra include [1]: The TWIST load spectrum, which represents the wing root bending moment of a transport aircraft [21], the FALSTAFF load spectrum [22], which represents the load-time history at the wing root of a fighter aircraft, and the WISPER load spectrum, which represents the flapwise bending of horizontal axis wind turbine blades [23]. Finally, only a few experimental approaches to VA fatigue make use of the stochastic VA loading spectra [3, 24, 25, 26].

The most common damage metrics in experimental studies of VA loading in FRP laminates are the number of load cycles to failure and/or the degradation of macroscopically observable specimen properties such as the residual strength and the residual stiffness. However, few experimental studies investigate the progression of the actual damage mechanism, e.g. delamination size or matrix crack density, under VA loading, which is of high interest to develop progressive damage models for VA fatigue. For example, within VA fatigue in FRP laminates, the evolution of matrix cracks is investigated in [5, 4, 27, 14], the crack growth in adhesively bonded joints is investigated in [19, 8, 28] and delamination growth is investigated in [29, 30, 31, 28]. Apart from few exceptions [31, 29], the growth rate of delaminations is rarely investigated under VA loading despite state-of-the-art prediction models are based on crack growth rate functions. Recent studies of delamination growth under two-level block loading [28, 29] reported a significant increase in crack extension in comparison to crack growth predictions that rely on fatigue properties obtained under CA loading. The increased crack extension in the VA tests in [29] are attributed to transient crack growth phenomena following the load amplitude changes, where the crack growth rate is significantly higher than CA baseline measurements of the crack growth rate. Digital image-based techniques and image processing algorithms proved to be well-suited in this regard to obtain a lot of data points and precise measurements of the delamination size and useful growth rate measurements during cyclic testing in a fully automated manner. Similar digital-image based techniques and image processing algorithms have proven to be well-suited for monitoring of the matrix crack density under VA loading [32, 27]. Furthermore, the complexity of the VA load spectra in studies of the fatigue delamination growth rate are limited to simple load sequence tests and two-level block loading tests, which are still unrepresentative for in-service loading. To help reducing this gap, experimental studies providing a more direct comparison between observations in simple block loading tests and VA loading spectra are encouraged.

One objective of the current work is to expand state-of-the-art delamination prediction models to improve simulation capabilities of VA fatigue. State-of-the-art simulation methods for delamination prediction, see e.g. reviews in [33, 34], involves correlation of the fatigue crack growth rate, da/dN, to an appropriate fracture mechanics parameter, e.g. the energy release rate, ERR, the J-integral, or the stress intensity factor, SIF, which has been measured under idealized CA loading conditions. Such relations will be referred to as Paris' law like relations in the following. In state-of-the-art delamination prediction models, it is assumed that the crack growth rate at a given time instant can be evaluated from the instantaneous values of e.g. the maximum ERR and the minimum ERR. This also applies to many state-of-the-art simulation methods for fatigue-driven delamination, e.g. fatigue cohesive zone models based on the envelope load approach [33], including the method presented in Deliverable D5.1 and Ref. [35]. A major concern in such approaches is the neglection of load interaction effects, which obviously contradicts the significant influence of the loading history on the crack growth rate as observed in experiments during VA fatigue [29, 31, 8].

To improve the prediction of crack growth under VA loading, the authors will include transient crack growth functions in the conventional crack growth rate functions based on the experimental work presented here and previous experimental work by the authors in Refs. [29, 31]. The procedure is illustrated in Fig. 1-4 and 1-5 below. Note the load spectra is illustrated in terms of the maximum applied ERR, G. According to conventional crack growth rate models, the crack growth rate, da/dN, during the multi-level block loading test in Fig. 1-4 will be piecewise constant as illustrated, because the model assumes that the crack growth rate, da/dN, is constant for a given level of maximum ERR, $\mathcal{G}$, corresponding to the Paris' law like relation. However, experimental evidences [29, 31] show that there is a transient behaviour following a step change in load amplitude that lasts several number of cycles before the CA baseline crack growth rate is achieved (Figure 1-5). Neglection of this transient behaviour leads to significant errors in the estimated delamination propagation. To overcome this situation, this work presents an extension of the delamination fatigue method in Ref. [35] by inclusion of transient crack growth responses at load amplitude changes.

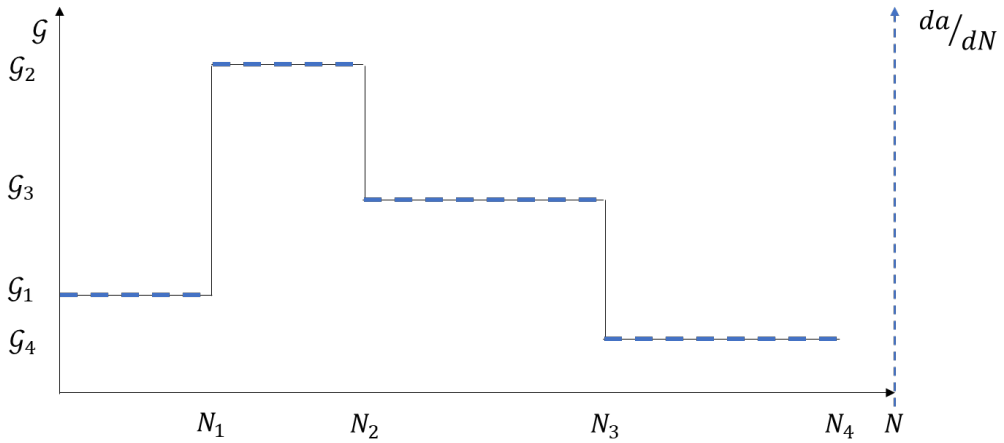

Figure 1-4. Crack growth rate during a multi-level block loading test assuming that the behaviour follows non-interaction Paris' law like relations.

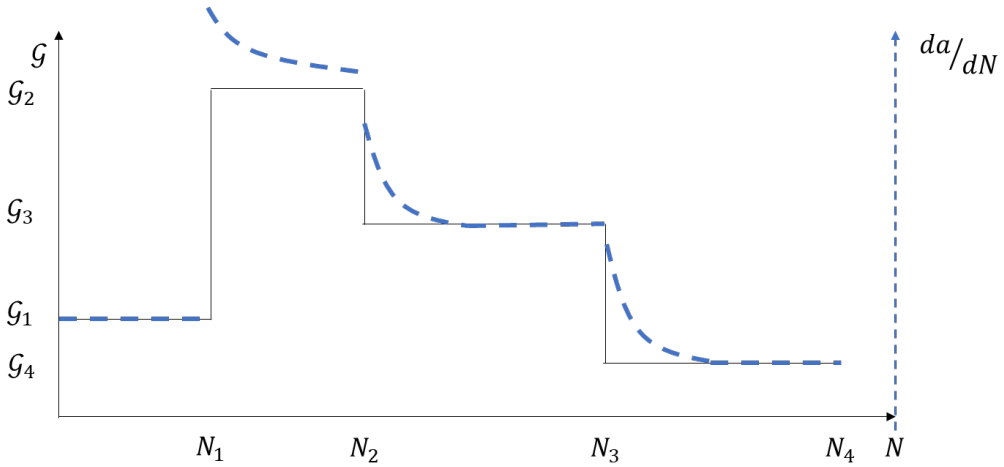

Figure 1-5. Transient crack growth rate after a load change followed by steady state behaviour.

2. Mechanical testing

This section explains the background, the methodology and the results of the mechanical testing part of Task 5.4. In the following, the term CA loading will refer to a cyclic varying ERR, G, with constant maximum and minimum value of the ERR. The term load amplitude change will refer to an amplitude change in the cyclic ERR. Low-to-high (LH) and high-to-low (HL) load amplitude changes are defined as illustrated in Fig. 2-1.

Here a transient phenomenon is defined as a crack growth response following a step change in load amplitude level that is different from the response measured during CA loading at the same maximum and minimum values of the applied energy release rate, ERR (or another governing fracture mechanics parameter). The transient crack growth responses will be characterized in terms of the crack growth rate, da/dN.

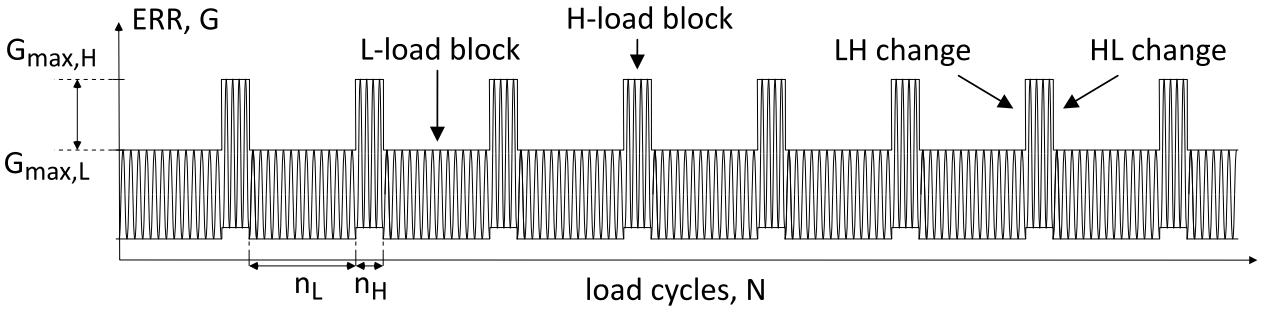

Figure 2-1: Two-level block loading. Definition of low to high (LH) changes and high to low (HL) changes.

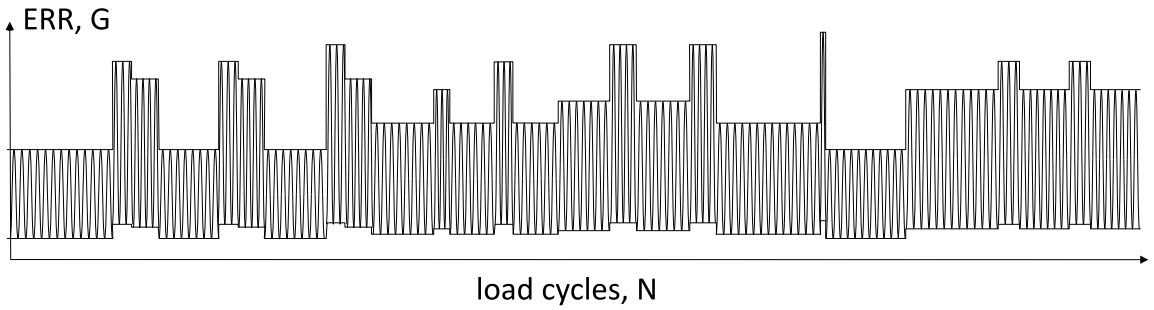

Figure 2-2: Multi-level block loading for demonstrator tests.

Work outline:

Subsections 2.1-2.3 present the material system and the new test fixture that has been developed to perform G-controlled cyclic testing of double cantilever beam (DCB) specimens. Subsections 2.4-2.5 explain the experimental methodology. The test campaign consists of two parts; firstly, the DCB specimens are subjected to two-level block loading as illustrated in Fig. 2-1 to characterize the transient crack growth phenomena following load amplitude changes and to identify model parameters of a new crack growth rate function. Secondly, the DCB specimens are subjected to a multi-level block loading spectrum, as illustrated in Fig. 2-2, to further investigate the transient crack growth phenomena when the applied load spectrum increases in complexity. The multi-level block loading test will also be a demonstrator for assessment of the new crack growth rate model for crack length predictions. Results from the experimental campaign are presented and discussed in subsection 2.7. Subsection 2.8 presents the new crack growth rate function for crack growth prediction under VA loading.

2.1. Material and specimen

The double cantilever beam (DCB) specimens are made of glass fiber reinforced epoxy with a unidirectional (UD1340) architecture based on non-crimp fabrics with backing fibers in the $\pm 45°$directions (BIAX100). The areal weight of the fiber mats is 1483 kg/m^2 with 7 wt% backing fibers. The DCB specimens have the following nominal dimensions: Length $L = 657$ mm, total height $2H = 8.2$ mm and width $W = 27.8$ mm. The artificial pre-crack has a nominal length of $a_0 = 100$ mm. The Young's modulus in the fiber directions is $E = 37.2$ GPa. The delamination propagates along a UD $0°/0°$ interface. The mode I fracture toughness (plateau value) is $G_c^{ss} = 1359$ J/m^2. Fiber bridging are observed in the wake of the crack tip.

2.2. Test rig for G-control cyclic tests

The experimental test campaign applies the pure moment loaded double cantilever beam (DCB) specimen as illustrated in Fig. 2-3. The applied bending moments, M, at the upper- and lower DCB arm are equal in magnitude but have opposite signs such that the delamination propagates under pure mode I crack opening. The path independent J-integral will be applied to compute the ERR, G:

$$G = J = \frac{(1-\kappa^2)M^2}{WE_1I} \qquad \text{Eq. 2-1}$$

Eq. 2-1 applies for an orthotropic laminate under plane strain conditions and mode I crack opening. E_1 is Young's modulus in the specimens longitudinal direction (i.e. fiber direction), κ is Possion's ratio, B is the specimen width, I is the area moment of inertia of the DCB arms $\left(I = \frac{1}{12}WH^3\right)$, and M is the applied bending moment as illustrated in Fig. 2-3. The applied ERR, G, is directly proportional to the squared value of the applied bending moment, M^2. Therefore, a M-controlled cyclic test is equivalent to a G-controlled cyclic test using the current test specimen configuration.

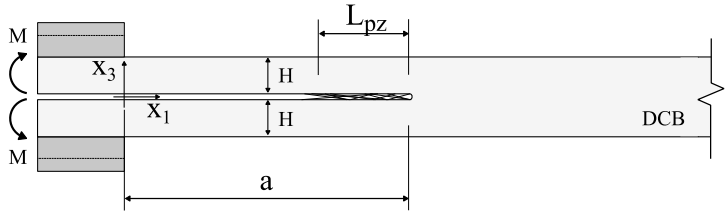

Figure 2-3: Pure moment loaded DCB specimen

To subject the DCB specimen to pure bending moments a new test fixture has been developed. The basic operating principle of the test fixture is schematically shown in 2D in Fig. 2-5 and a real photograph of the test fixture is shown in Fig. 2-4. The test fixture uses the same basic principle as applied in [36] for cyclic testing of aluminium adherents bonded by epoxy-adhesive. The basic operating principle of the test fixture has been modified to enable cyclic testing of compliant DCB specimens, e.g. laminated GFRP DCB specimens, in G-control. The modifications will be described in the remaining of this subsection.

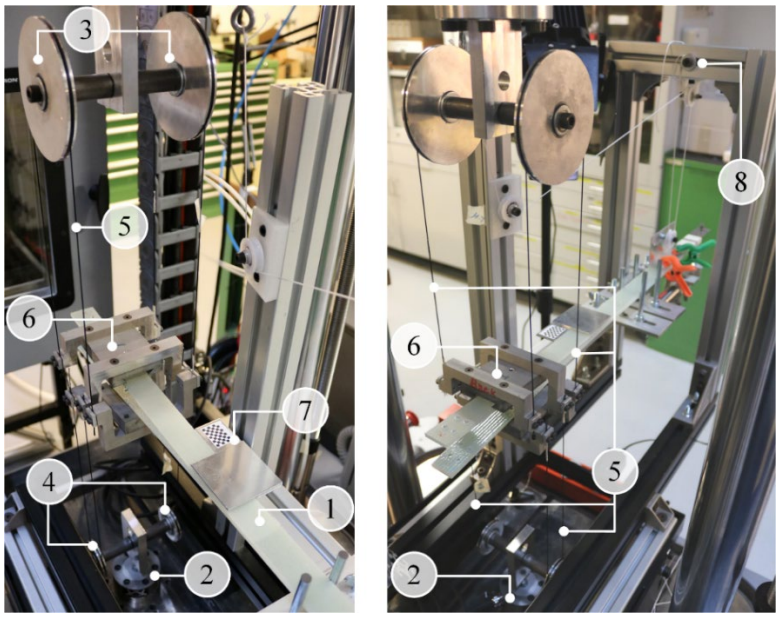

Figure 2-4: Photography of the test fixture. Annotations: 1: DCB specimen; 2: Load cell; 3: upper wheels; 4: Lower wheels; 5: Teflon coated steel wire; 6: Loading blocks; 7: Checkerboard pattern; 8: Specimen support structure;

Pure bending moments are applied to the DCB specimen through a wire pulley system as illustrated in Fig. 2-4 and Fig. 2-5. The load string comprises the DCB specimen, a dynamic 2kN rated Instron load cell, the upper- (radius $R = 60.0$ mm) and lower (radius $r = 40.0$ mm) wheels, four Teflon-coated steel wires of diameter $d = 1.1$ mm, and two loading blocks, which are directly attached to the tabs of the DCB specimen. The upper wheels are attached to a linear actuated piston from a computer-controlled electric Instron test machine (E10000 system). The lower wheel is kept fixed and directly connected to the load cell which is attached to the load frame table of the test machine as shown in Fig. 2-4. The upper- and the lower wheels may rotate with negligible friction using low friction hybrid ceramic bearings. A support structure is installed to ensure that the longitudinal center axis of the DCB specimen remains horizontal as the piston translates.

The test machine's crosshead displacement is equal to the displacement of the upper wheels, which will be denoted by v in the following. The rotations of the upper- and lower loading blocks are symmetric and the angles of rotation will be denoted by θ. The force couples of magnitude, $F/2$, which act at the upper- and lower DCB arm as indicated in Fig. 2-6, comprises the applied bending moment, M. The moment arm of the force couple reduces as the DCB arms rotate, which is illustrated in Fig. 2-5 and by the following equation:

$$M = \frac{F(R+r)}{2}\cos\theta = \frac{F(R+r)}{2} f(v) \qquad \text{Eq. 2-2}$$

The applied bending moment becomes a function of the angle of rotation, θ, and the applied force, F, i.e. $M(F,\theta)$. A simple kinematic relation can be derived between the angle of rotation, θ, and the displacement, v: $\theta = p(v)$, such that the applied bending moment can be rewritten to be a function of the form seen on the right-hand side in Eq. 2-2, i.e. $M(F,\theta) \Rightarrow M(F,v)$, where $f(v) = \cos(p(v))$.

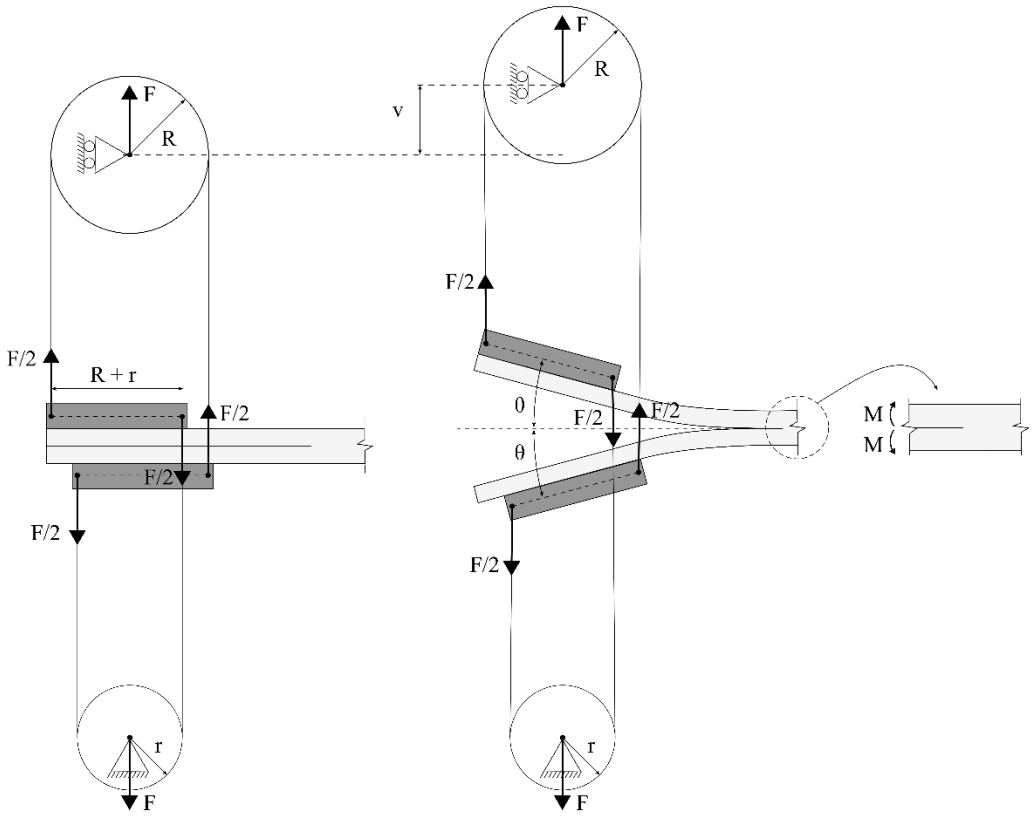

Figure 2-5: Schematic outline of the load introduction to the pure moment loaded DCB specimen.

The kinematic relation $p(v)$ is derived from an experiment of simultaneous measurements of the cross head displacement, v, and the angle of rotation, θ, which has been measured using an inclinometer. The measurements are shown in Fig. 2-6. The curve fit is based on a suitable range of the displacement $v \in [0; 20]$ mm that may be experienced in the cyclic tests. The relation applies for the current test fixture configuration and is independent of the crack length. Substituting Eq. 2-2 in Eq. 2-1 the applied ERR, G, becomes:

$$G(F, v) = \frac{(1-\kappa^2)}{BE_1 I}\left(\frac{F(R+r)}{2}\right)^2 f(v)^2$$	Eq. 2-4

Where $f(v) = \cos(p(v))$. Fig. 2-6 shows graphs for the function $f(v)$. The right axis in Fig. 2-6(right) shows the value $\epsilon = 1 - f(v)^2$ which is a measure of the error introduced by neglecting the changing moment arm as the loading blocks rotate, i.e. assuming that $M(\theta, v) \approx M(F)$. For example, an error of $\epsilon = 5\%$ and $\epsilon = 10\%$ in the applied ERR, G, will be encountered for a crosshead displacement of $v = 13.7$ mm and $v = 18.5$ mm, respectively. This error has a significant effect on the crack growth rate in fatigue.

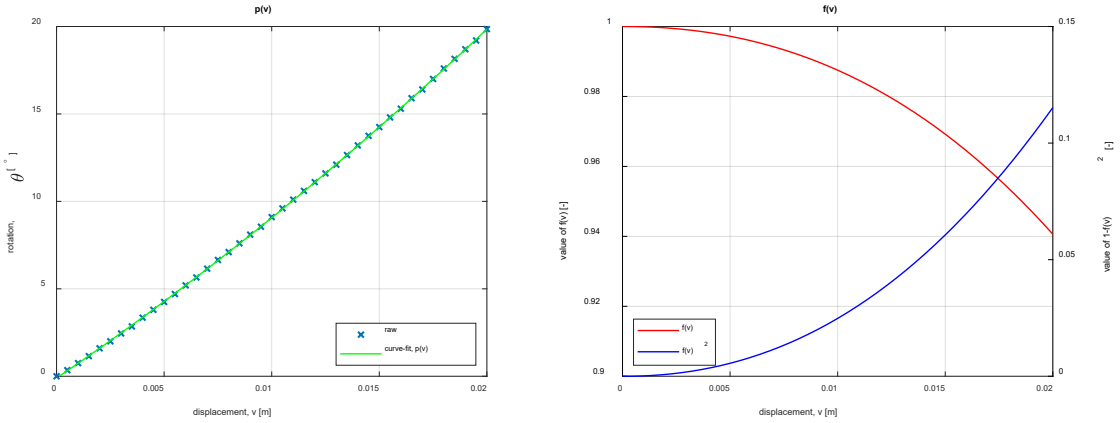

Figure 2-6: Left: Kinematic relations to establish a relation between the cross head displacement and the angle of rotation. Right: Graph for $\boldsymbol{f(v) = \cos(p(v))}$ from Eq. 1.

To perform M – controlled cyclic tests (equivalent to G-controlled cyclic tests cf. Eq. 2-1) the controller of the test machine needs to generate a controllable channel by combining signals from two physical source transducers: The force transducer to measure F and the position transducer to measure v. This can be accomplished using user-defined channel calculations and advanced amplitude control options in the *Instron WaveMatrix2* software.

2.3. G-controlled VA testing

The test fixture will be applied for VA loading such that the applied bending moment, M, (equivalently the ERR, G) is prescribed according to load spectra similar to those illustrated in Fig. 2-1 and Fig. 2-2. The crack growth immediately after the load amplitude changes is of particular interest in the current work, which makes it relevant to evaluate the response of the prescribed value when changes in loading conditions occur. Figure 2-8 shows the relative error between the target signal and the measured signal following LH- and HL step changes in load amplitude level during a two-level block loading test. Within $\Delta N = 20$ load cycles the relative error is decreased to less than 1%. The target value is reached within $\Delta N = 40$ and $\Delta N = 50$ load cycles following the LH and the HL load amplitude change, respectively. Notice that the responses approach the target values from below in both cases.

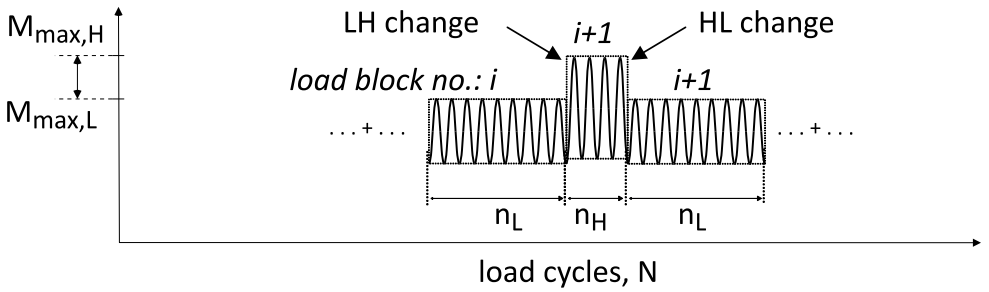

Figure 2-8: Illustration of a low to high (LH) load amplitude change and a high to low (HL) load amplitude change in block loadng tests**.** The squared value of the applied bending moment, $\boldsymbol{M}$, is directly proportional to the applied ERR, $\boldsymbol{G}$.

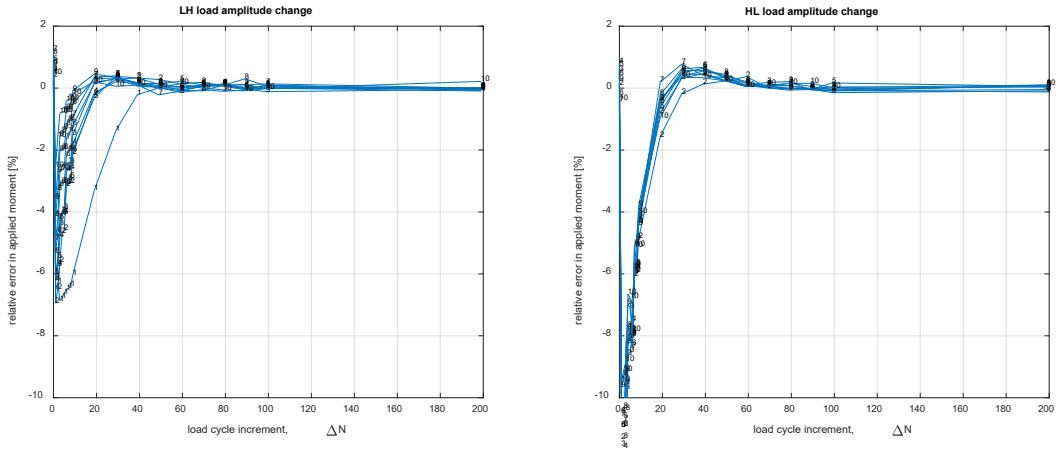

Figure 2-9: The relative error ($\left(\left(\boldsymbol{M_{actual}} - \boldsymbol{M_{target}}\right)/\boldsymbol{M_{target}}\right) * \mathbf{100}$) in the max value of the applied bending moment, $\boldsymbol{M_{max}}$, following LH load amplitude changes (left) and HL load amplitude changes (right) in a two-level block loading experiment with repeated L- and H-blocks. The number annotations refers to the load block number (i.e. $\boldsymbol{i}$ in Fig. 2-8)

The applied bending moment during the demonstrator test is also investigated. The response is similar to what is observed in Fig. 2-9. The applied bending moment approach the maximum target value, M_{max}, from below. Within $\Delta N = 20$ and $\Delta N = 40$ load cycles the error between the actual value of M_{max} and the target value is approximately 1% and negligible, respectively. Similar responses are observed across all magnitudes of step change in load level in the demonstrator test.

2.4. Crack length growth rate measurements

The crack length, a, is measured using an automated digital-image based technique that has been developed in [37] for tracking of the crack fronts in translucent materials. The method will be referred to as the crack tracking algorithm in the following. The crack tracking algorithm has been applied in recent studies of fatigue-driven delamination under VA loading in [31, 29]. The basic principle of the method is a correlation between the crack front and the diffuse reflected light in translucent materials such as glass/epoxy laminates. In the very early stages of damage, an increased intensity of diffuse reflected light occurs due to crack face separation and the irregular surface of newly formed cracked area such that damaged and undamaged regions can be visually identified [37]. The method can identify the position of the crack front across the specimen width from digital images and application of a series of image processing operations. The crack length, a, is defined here as the average crack length across the specimen width. The authors would like to highlight that the method identifies the position of the crack front, i.e. a in Fig. 2-3, and bridging fibres will appear in the wake of the crack front.

The methods uses the following hardware: A monochrome FLIR Blackfly CCD type camera with a resolution of 2448x2048 pixels, two cool LED white light sources NILA Zaila Daylight to illuminate the top surface of the DCB specimen, and a computer for image acquisition and storage. Images are acquired at a predefined cycle increment ΔN_{im}, which controls the temporal resolution of the crack length measurements. The process is fully automated and continuous without interruption of the cyclic test. The camera records the top surface of the DCB specimen. The camera's field of view (FOV) is illustrated in Fig. 2-12. The FOV includes the region of interest (ROI) with respect to crack length measurements and a checkerboard, which is necessary for the crack tracking algorithm (reference pattern, image transformations etc.). The crack tracking algorithm outputs the average crack length, a, across the specimen width as a function of the number of load cycles, N. The resolution of the average crack length across the specimen width is 0.05 mm in the current test campaign. The crack growth rate, da/dN, is computed for every data point in the (N, a)-data set by fitting a linear function to all data points within a moving fitting window that has been centred around

the data point of interest as described in [37]. When the applied load pattern is two- or multi-level block amplitude loading, the crack growth rate, da/dN, is computed for every load block separately.

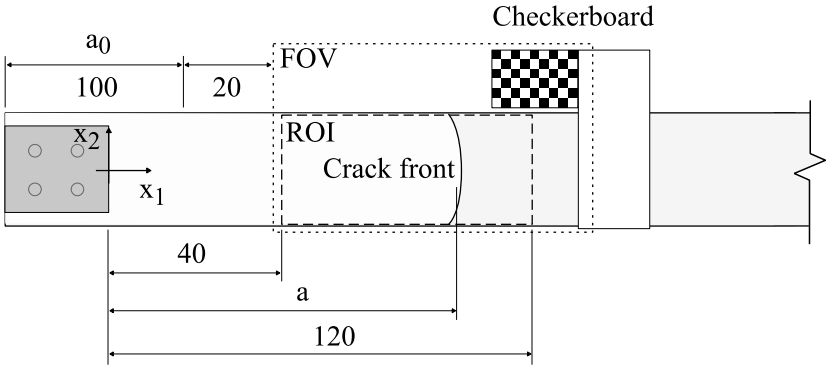

Figure 2-12: Illustration of the DCB specimen seen from above. Note the crack length, $\boldsymbol{a}$, is actually the average crack length across the specimen width. FOV: Field of view. The crack length is measured in region of interest (ROI). Dimensioning lines are not drawn to scale.

Note that the ROI does not start at the artificial pre-crack, a_0. In every test the crack is propagated in fatigue for at least 20 mm of crack extension before the crack front reaches the ROI. During this phase the applied ERR corresponds to the ERR of the first load block in the actual fatigue test. This procedure is followed to ensure a natural pre-crack and a fully developed fiber bridging zone at the beginning of the ROI.

2.5. Test matrix

Tab. 1 gives an overview of the cyclic tests. The cyclic tests may contain a single load block or multiple load blocks. The cyclic tests can be divided into three main types: Constant amplitude tests (denoted by CA in the test ID), two-level block loading tests similar to Fig. 2-1 (denoted by BL in the test ID), and multi-level block loading demonstrator tests (denoted by DEM in the test ID). All cyclic tests are performed in G-control. The applied bending moment will be expressed as a fraction of the fracture toughness of the material system $G_c^{ss} = 1.36\ kJ/m^2$. A scalar, γ, is introduced such that the applied ERR, G_{app}, can be expressed relative to the plateau fracture toughness as indicated here:

$G_{app} = \gamma G_c^{ss}$	Eq. 2-5

The applied bending moment, M_{app}, may also be expressed in terms of the scalar γ since $M^2 \propto G$ cf. Eq. 2-1:

$M_{app} = \sqrt{\gamma} M_c^{ss}$	Eq. 2-6

Where the plateau moment $M_c^{ss} = 15.1$ Nm cf. Eq. 2-1 for the current specimen geometry and material properties. The applied bending moments are listed in Tab. 1 for the various cyclic tests. A load ratio of $R = M_{min}/M_{max} = 0.2$ is kept in every load block of all the cyclic tests. The demonstrator test is a multi-level block loading spectrum as illustrated in Fig. 2-2. Tab. 2 shows further details on the applied load spectrum for the demonstrator test. Results from the CA, BL, and DEM tests will be presented in the following.

Test ID	$\gamma_{L,max}$	$\gamma_{H,max}$	Applied moment M_{app} [Nm], R=0.2	ΔN_{im} $[cyc]$
T01B03BL3060	0.305	0.610	$M_{L,max} = 8.27; M_{H,max} = 11.70;$	10
T02B02BL3075	0.305	0.762	$M_{L,max} = 8.27; M_{H,max} = 13.08;$	10
T05B05CA30	0.305	-	$M_{max} = 8.27;$	100
T06B07CA30	0.305	-	$M_{max} = 8.27;$	100
T07B10BL3050	0.305	0.510	$M_{L,max} = 8.27; M_{H,max} = 10.70;$	10
T08B09CA50	0.510	-	$M_{max} = 10.70;$	50
T09B04CA60	0.610	-	$M_{max} = 11.70;$	20
T10B06CA75	0.762	-	$M_{max} = 13.08;$	10
T11B05DEM01	-	-	-	10
T12B02DEM02	-	-	-	10
T13B08BL3085	-	0.864	$M_{L,max} = 8.27; M_{H,max} = 13.92;$	10

Table 1: Test matrix showing the test ID and the applied load pattern. The parameter ΔN_{im} is the cycle increment for crack length measurements.

Load block number	$\frac{G_{max}}{G_c^{ss}}$	*Max applied bending moment* M_{max} *[Nm], R=0.2*	*Number of load cycles* N $[cyc]$
1	0.305	8.27	20,000
2	0.711	12.63	400
3	0.610	11.70	1,500
4	0.305	8.27	15,000
5	0.711	12.63	400
6	0.610	11.70	1,500
7	0.305	8.27	15,000
8	0.762	13.08	400
9	0.610	11.70	1,500
10	0.457	10.13	10,000
11	0.559	11.20	1,000
12	0.457	10.13	5,000
13	0.711	12.63	200
14	0.457	10.13	5,000
15	0.510	10.70	3,000
16	0.762	13.08	300

17	0.510	10.70	3,000
18	0.762	13.08	300
19	0.457	10.13	5,000
20	0.915	14.33	50
21	0.305	8.27	15,000
22	0.559	11.20	2,000
23	0.711	12.63	300
24	0.559	11.20	2,000
25	0.711	12.63	300
26	0.559	11.20	2,000
Total cycles:			110,150

Table 2: Details on the applied load blocks during the multi-level block loading test.

2.6. Results: CA loading and Paris' law

Figure 2-13 shows a graph of the crack growth rate, da/dN, versus the crack length, a, for the constant G-tests T05B05CA30 and T06B07CA30 at $\gamma = G_{max}/G_c^{ss} \approx 0.3$. The crack growth rate is approximately constant in both tests as expected according to Paris' law like relations. The mean value of the crack growth rate is $da/dN = 4.60 \cdot 10^{-5}$ mm/cyc and is denoted as the *global mean* in Fig. 2-13. The standard deviation is on the order of $2\sigma \approx \pm 3.4 \cdot 10^{-5}$ mm/cyc.

Several constant G-tests are conduced at different values of the maximum ERR, G_{max}, at constant load ratio $R = 0.2$. The corresponding crack growth rates are reported in Fig. 2-14 on log-log axes. A nonlinear least squares fit is generated to characterize parameters of Paris law on the following form:

$$\frac{da}{dN} = A\left(\frac{G_{max}(1-R)}{G_c^{ss}}\right)^p \qquad \text{Eq. 2-7}$$

Where parameters $A = 0.0727$ and $p = 5.13$ have been computed.

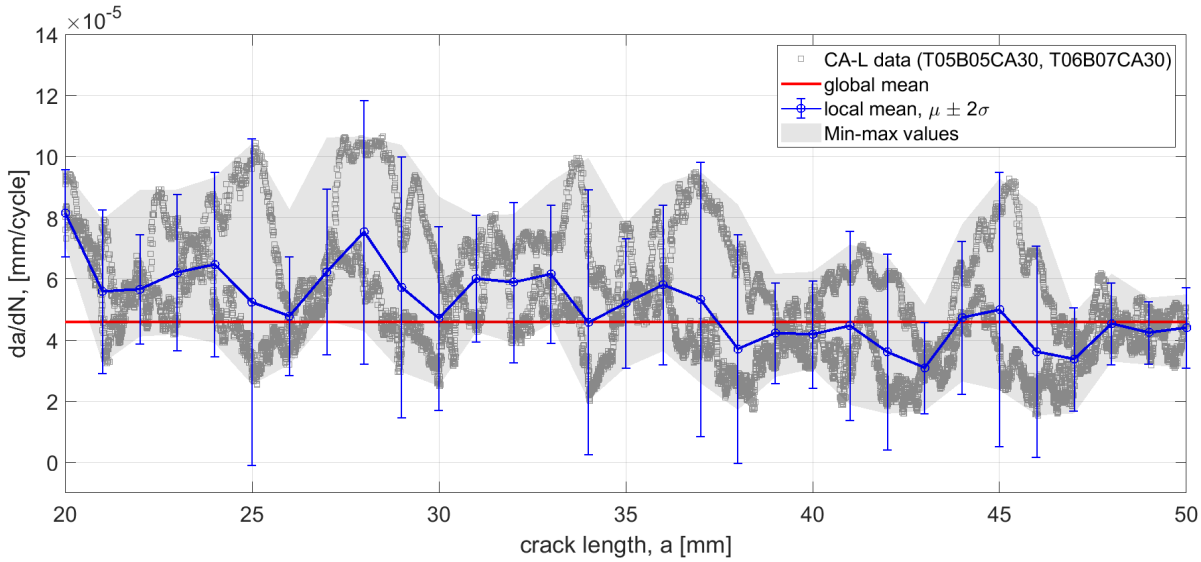

Figure 2-13: Crack growth rate versus crack length of CA30 tests. The global mean is computed as the mean value of $\boldsymbol{da/dN}$ over the entire range $\boldsymbol{a} = [\mathbf{20}; \mathbf{50}]$ mm. The local mean is computed within every 1 mm of crack extension which contains approximately 320-480 data points. A reasonable agreement between the local and global mean values is observed as expected.

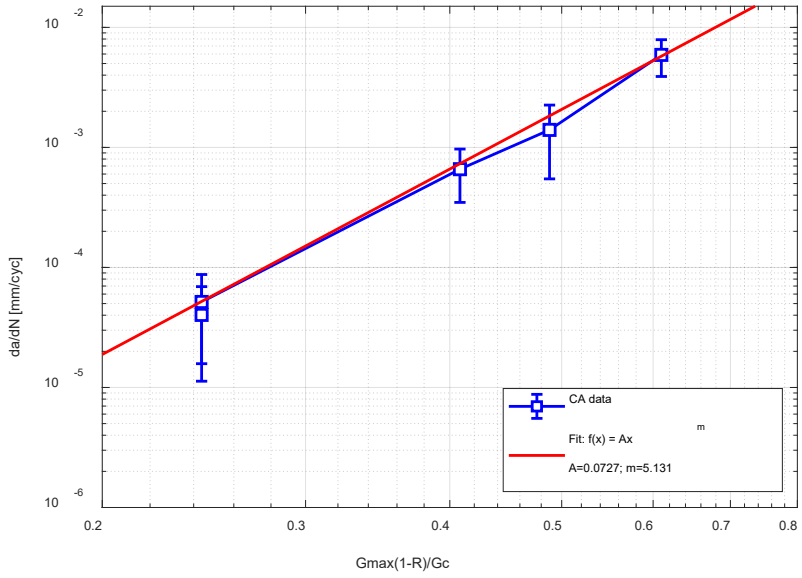

Figure 2-14: Correlation between the crack growth rate, $\boldsymbol{da/dN}$. and the maximum applied ERR, $\boldsymbol{G_{max}}$, on log double logarithmic axes. The curve fit yields Paris' law parameters.

The measured crack growth rate in constant G-tests using the pure moment loaded DCB test configuration is a steady-state response in the sense that the crack tip propagates in a self-similar fashion at a constant crack growth rate, and the fully developed FBZ maintains its size and translates along the crack tip in a self-similar manner [38, 29]. The crack growth rates that have been measured in the constant G-tests will be considered as a steady-state response and will be used as baseline measurements in the following to investigate the crack growth rate under VA loading.

2.7. Results: Two-level block amplitude loading

The two-level block loading tests consist of repeated high (H) and low (L) load blocks as illustrated in Fig. 2-15. A total of four two-level BL tests are performed. The maximum ERR of the L-load blocks are kept constant $G_{max,L} = 0.3G_c^{ss}$ while the maximum ERR of the H-load blocks, $G_{max,H}$, is varied across the four BL tests. A graph of the crack length, a, versus the number of load cycles, N, is exemplified for the BL3075 test in Fig. 2-15. A similar response is observed for the remaining BL tests. The data is divided into H- and L-load blocks and grouped depending on the load block number. The green annotations in Fig. 2-15 denotes the load block numbering.

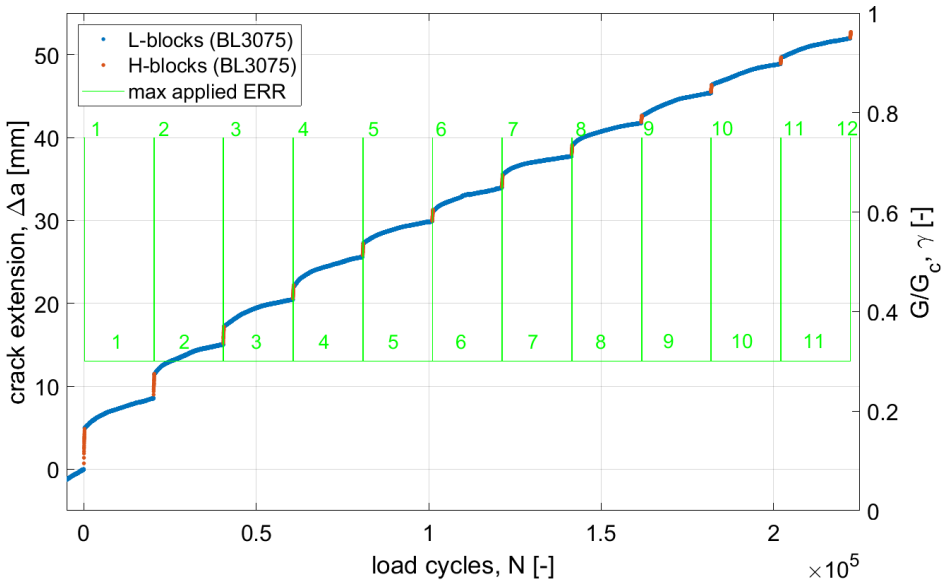

Figure 2-15: Left axis: Crack extension versus number of load cycles in two-level block amplitude loading. Right axis: Max applied ERR (normalized wrt. plateau fracture toughness) versus number of load cycles.

The two-level BL tests include several consecutive low to high (LH) and high to low (HL) load amplitude changes. For every H- and L-load block the crack extension, Δa, and the crack growth rate, da/dN, can be plotted as a function of the load cycle increment ΔN following the load amplitude change. This generates a series of response curves superimposed on top of one another, which enables a direct comparison between arbitrary load block numbers. Examples are provided in Fig. 2-18(a)-(d) and 2-19(a)-(d) for the BL3075 test and the BL3060 test, respectively. The number-symbols on the graphs indicates the load block number. The subfigures (a) and (c) shows the crack growth response following the LH load amplitude changes whereas figures (b) and (d) shows the crack growth response following HL load amplitude changes. In the L-load blocks a characteristic transient crack growth behaviour is observed following the HL load amplitude changes. A similar transient crack growth behaviour has recently been observed in [29] for another glass/epoxy material system. Immediately after the HL load amplitude change, a relatively high crack growth rate is observed followed by a steep descend in the crack growth rate until it approaches the CA baseline. The short duration of the H-load blocks makes it difficult to characterize transient crack growth phenomena. However, the crack growth rate during the H-load blocks clearly decreases as the number of H-load cycles increases. Similar tendencies have been observed for all the BL tests.

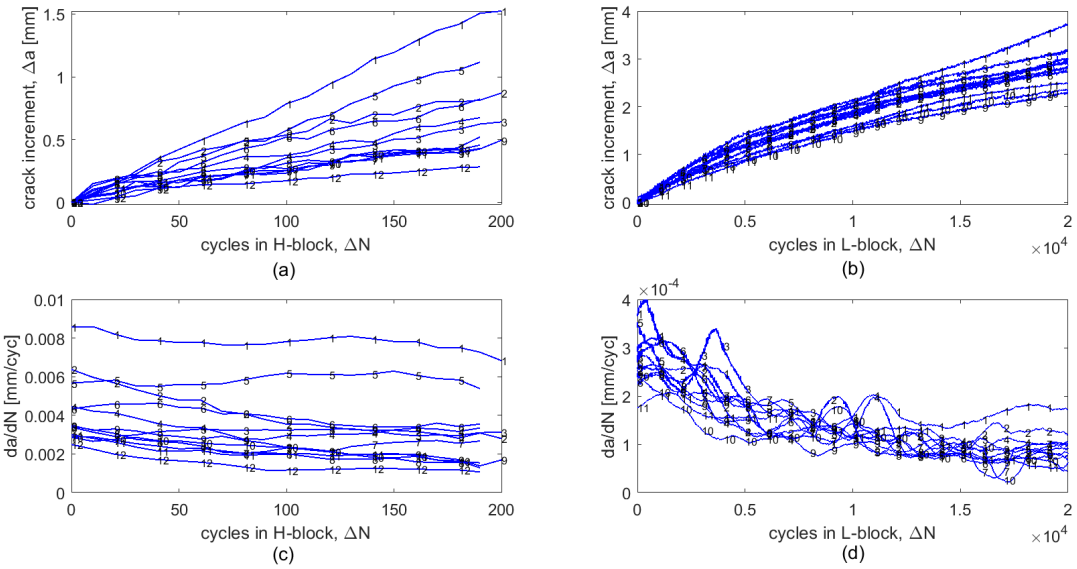

Figure 2-18: Data for the BL3075 test. The crack extension, $\boldsymbol{\Delta a}$, and the crack growth rate, $\boldsymbol{da/dN}$, within an arbitrary load block is plotted against the load cycle increment, $\boldsymbol{\Delta N}$, following load amplitude change. Fig. (a) and Fig. (c) show the response curves during the H-load blocks of the BL test. Fig. (b) and Fig. (d) show the response curves during the l-load blocks of the BL test. The numbers in the graphs refer to the load block number cf. Fig. 2-1.

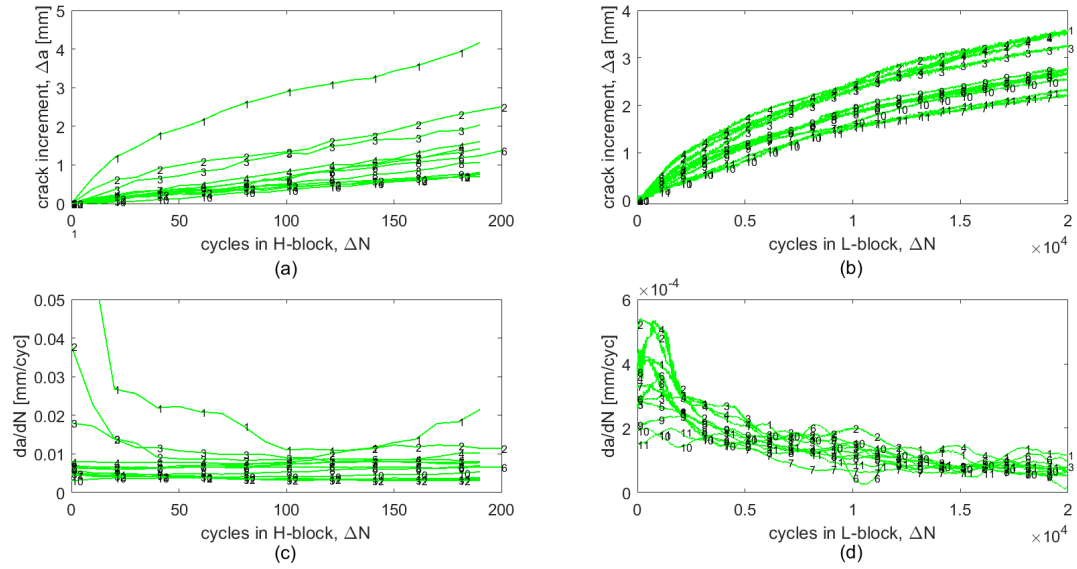

Figure 2-19: Data for the BL3060 test. The crack extension, $\boldsymbol{\Delta a}$, and the crack growth rate, $\boldsymbol{da/dN}$, within an arbitrary load block is plotted against the load cycle increment, $\boldsymbol{\Delta N}$, following load amplitude change. Fig. (a) and Fig. (c) show the response curves during the H-load blocks of the BL test. Fig. (b) and Fig. (d) show the response curves during the l-load blocks of the BL test. The numbers in the graphs refer to the load block number cf. Fig. 2-1.

2.8. Results: Transient crack growth following HL load amplitude changes

The transient crack growth rate during the L-load blocks appears to repeat whenever a HL load amplitude change has occurred, cf. Fig. 2-18(d) and Fig. 2-19(d). In the following, the transient crack growth rate following the HL load amplitude change is assumed to be independent of the load block number. A curve fit is established for every BL test to describe the transient crack growth response at the HL load amplitude change. The curve fits are based on the crack growth rate measurements following the HL load amplitude changes as exemplified for the BL3075 test and the BL3060 test in Fig. 2-18(d) and Fig. 2-19(d), respectively. The curve fitting function is assumed to be an exponential decaying function of the following form:

$da/dN = f(\Delta N) = D\exp(-m\Delta N) + C$	Eq. 2-8

The curve fits are generated by nonlinear least squares methods. The parameter D in Eq. 2-8 governs the crack growth rate immediately after the HL-load ampliude change ($\Delta N = 0$) and the decay constant m determines the rate of decay of the transient response. The parameter C express the crack growth rate by the end of the transient phase and should match the crack growth rate measured under CA loading (steady-state). The parameter C is assumed to be equal to the CA baseline (the steady-state value) as computed by Paris law in Eq. 2-7. The resulting curve fits are shown in Fig. 2-20 for each of the four BL test.

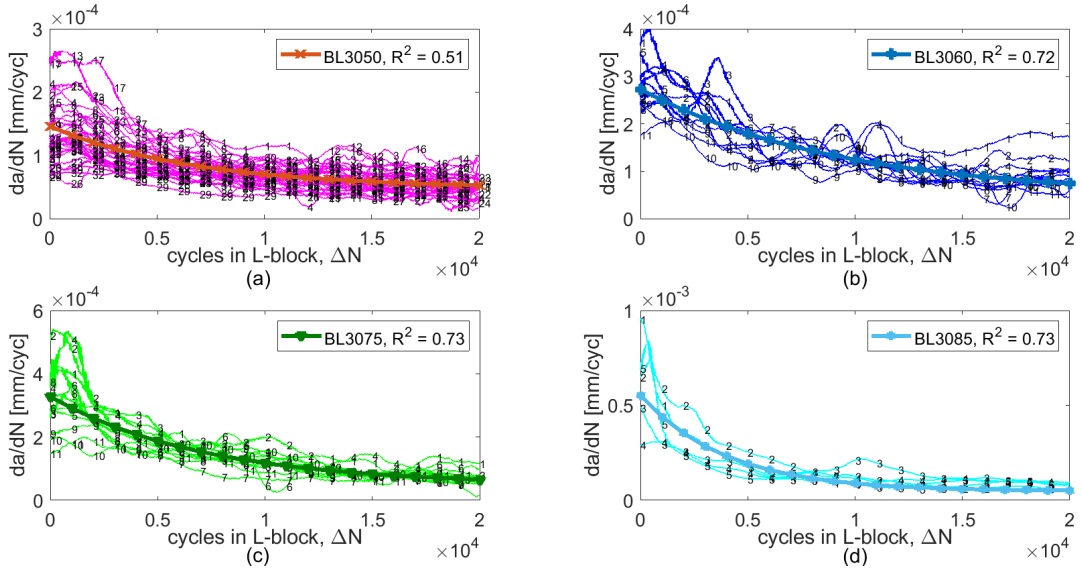

Figure 2-20: Superimposing the transient crack growth rate following every HL load amplitude change in the two-level block amplitude loading tests. Top-left: BL3050. Top-right: BL3060. Bottom left: BL3075. Bottom right: BL3085. Least squares curve-fits are included for every test.

The curve fits are compared in Fig. 2-21, which plots the parameters $B = \frac{D}{C}$ and m of the exponential decay function against the step change in the maximum applied ERR between the H- and L-load blocks: $\Delta G_{max} = G_{H,max} - G_{L,max}$. The parameter $B = \frac{D}{C}$ expresses the overshoot in the crack growth rate immediately after the HL load amplitude change (i.e. at $\Delta N = 0$) normalized with respect to the CA baseline crack growth rate. Fig. 2-20 and Fig. 2-21 clearly show that the transient crack growth rate due to a HL load amplitude change increases as ΔG_{max} increases. A second order polynomial fit is generated for the relationship between the parameter B and the step change in maximum ERR, ΔG_{max} as shown in Fig. 2-21. The resulting equation is given here:

$B(\Delta G_{max}) = \frac{D}{C} = p_{1B}\left(\frac{\lvert\Delta G_{\max}\rvert}{G_c^{ss}}\right)^2 + p_{2B}\left(\frac{\lvert\Delta G_{\max}\rvert}{G_c^{ss}}\right) + p_{3B}$ Where $p_{1B} = 20.99; p_{2B} = 6.24; p_{3B} = 0;\ R^2 = 0.955$	Eq. 2-9

A linear function is fitted to the relationship between the decay constant, m, of the exponential function and the step change in load amplitude level, ΔG_{max}, as illustrated in Fig. 2-21 and Eq. 2-10.

$$m(\Delta G_{max}) = p_{1m}\left(\frac{|\Delta G_{\max}|}{G_c^{ss}}\right) + p_{2m}$$

Where $p_{1\tau} = 2.771e-4;\ p_{2\tau} = 5.8e-5;\ R^2 = 0.388$

Eq. 2-10

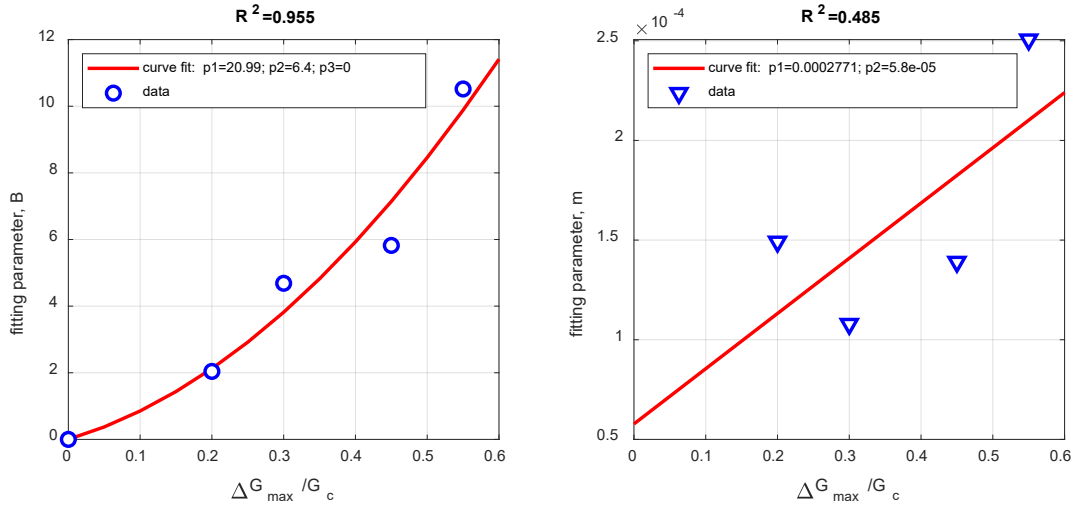

Figure 2-21: Comparison of curve fitting parameters, $\boldsymbol{B = D/C}$ and the decay constant, $\boldsymbol{m}$, for the curve fits describing the transient crack growth following HL load amplitude changes.

2.9. Crack growth rate functions

The conventional non-interaction model:

A crack growth prediction can be obtained by direct summation of crack increments caused by each load cycle. A common approach is to assume that the crack growth increment, Δa_i, associated with a given cycle of variable amplitude loading can be estimated from CA data and Paris' law, for example the relation $f(G_{max}, R)$ in Eq. 2-7, such that:

$$a_N = a_0 + \sum_{i=1}^{N_{tot}} f(G_{max,i}, R_i) = a_0 + \sum_{i=1}^{N_{tot}} \left(A\left(\frac{G_{max,i}(1-R_i)}{G_c^{ss}}\right)^p\right)$$

Eq. 2-11

Where a_0 is the starting crack length, N_{tot} is the total number of load cycles and a_N is the crack length after N_{tot} load cycles. This model assumes that the current crack increment can be evaluated from the instantaneous value of the cyclic load parameters $(G_{max,i}, R_i)$ at a given load cycle, N_i, and thereby neglects any influence of the load history. This type of model is also known as a non-interaction model as load interaction effects are neglected. A similar practice is exercised in the majority of state-of-the-art delamination prediction models, e.g. fatigue cohesive zone models [33]. The non-interaction model has been applied to simulate the crack growth during the VA load spectrum of the demonstrator test. The results are included in Fig. 2-22 – Fig. 2-23 by the red graphs.

A new crack growth rate model including load interaction effects:

The new crack growth rate model is an interaction crack growth rate model as it includes information of the load history on the current crack growth rate. Only the transient crack growth following HL load amplitude changes will be included in the current model. The crack growth response following LH load amplitude changes remains unchanged with respect to the conventional non-interaction model.

The basic approach of the new crack growth rate model is to compute the current crack growth rate, da/dN, as the superposition of two terms, which will be denoted as the steady-state term, da/dN_{ss}, and the transient term, da/dN_{tr}:

$$\frac{da}{dN} = \frac{da}{dN_{ss}} + \frac{da}{dN_{tr}} \qquad \text{Eq. 2-12}$$

The first term is a steady-state crack growth rate, da/dN_{ss}, which corresponds to the CA baseline crack growth rate. The steady-state term is a non-interaction term in the sense that the current value depends only the instantaneous value of the cyclic load parameters, such that the term can be evaluated from Eq. 2-7. The second term is a transient crack growth rate, da/dN_{tr}. The transient term will be zero by default and becomes non-zero if a HL load amplitude change has occurred. The transient term goes to zero with increasing number of load cycles. The transient term depends on the current cyclic load parameters and the load history, i.e. the term is an interaction term. The above has been summarized in the following two equations:

$$\frac{da}{dN_{ss}} = A\left(\frac{G_{max}(1-R)}{G_c^{ss}}\right)^p \qquad \text{Eq. 2-13}$$

$$\frac{da}{dN_{tr}} = \begin{Bmatrix} 0 \\ T_{HL} \end{Bmatrix} \quad \begin{matrix} for\ conditions\ I) \\ for\ conditions\ II) \end{matrix} \qquad \text{Eq. 2-14}$$

Where the transient term will attain one of the two functions in Eq. 2-14 depending on the following conditions I and II:

- Condition I: CA loading and crack growth following a LH load amplitude change.
- Condition II: Crack growth following a HL load amplitude change.

The transient function, T_{HL}, for the HL load amplitude change, will apply the trends and equations derived in Sec. 2-8. The exponential decay term of Eq. 2-8 is the basis of the transient function, and the relations derived in Eq. 2-9 and Eq. 2-10 will be imposed. The transient function becomes:

$$T_{HL} = \bar{B}\exp(-\bar{m}\,\Delta N)\left(\frac{da}{dN_{ss}}\right) \qquad \text{Eq. 2-15}$$

Where $\bar{B}$ is the overshoot crack growth rate relative to the CA baseline immediately after the HL load amplitude change ($\Delta N = 0$) value and $\bar{m}$ is the decay constant. The equations in Sec. 2.9 (for parameters B and m) are derived for a fixed value of the maximum ERR of the L-load block ($G_{max,L} = 0.3G_c^{ss}$). Modifications of Eq. 2-8 to Eq. 2-10 are necessary to generalize the equations to arbitrary load levels. The parameter $\bar{B}$ will be defined identical to B in Eq. 2-9:

$$\bar{B} = B \qquad \text{Eq. 2-16}$$

The decay constant, $\bar{m}$, will be different from the decay constant, m, in Eq. 2-10. The decay constant $\bar{m}$ will depend on the crack growth rate at the L-load level following the HL-load amplitude change:

$$\bar{m} = \left(\frac{C}{\frac{da}{dN_{ss}}} \right) m \qquad \text{Eq. 2-17}$$

Where the parameter $C = 4.60e-5$ mm/cyc (see Sec. 2-8) and represents the CA baseline crack growth rate at the L-load level that has been used to measure the decay constant m in Eq. 2-10 from two-level block loading tests. The scaling ensures that the duration of the transient phase reduces when the crack growth rate, da/dN_{ss}, at the L-load level of an arbitrary HL load amplitude change is higher than the CA baseline crack growth rate C in Sec. 2-9.

To simulate delamination growth for the demonstrator test it is assumed that the values of parameters B and m can be inter- and extrapolated in the range $0.0 \leq G_{max}/G_c^{ss} \leq 0.6$. The new crack growth rate model is formulated in terms of load blocks of arbitrary duration. The transient term will reset when a new load block is encountered. The model formulation relies on a block-wise definition of the applied load spectra. Hence, the approach is most suited for multi-level block loading spectra or VA load spectra that can be naturally divided into multi-level block loading spectra (load blocks of arbitrary duration), which may require pre-processing of the VA load spectra.

2.10. Results: Demonstrator VA test

The crack extension, Δa, is plotted against the number of load cycles, N, for the demonstrator tests in Fig. 2-22 on the left axis. The maximum applied ERR in the demonstrator tests is shown in the same figure on the right axis. Two repetitions of the demonstrator tests has been performed. Note a limited range of data is available for the *T12DEM02* test as it stopped prematurely due to fracture of a wire in the test fixture at the 20th load block. The demonstrator tests DEM01 and DEM02 displays similar trends. However, a relatively large difference occurs at load block no. 2-3, which causes an offset throughout the remaining of the tests.

A large amount of crack extension occurs in the high load level load blocks: 2, 3, 5, 6, 8 and 9. Although load block pairs 2-3 and 5-6 are identical, there is a difference in the amount of crack growth. The initial “H”-load blocks cause more damage than later “H” load blocks. The observation is consistent with the observations in Fig. 2-18(a),(c) and Fig. 2-19(a),(c) in Sec. 2.7.

The crack growth rate, da/dN, during the demonstrator tests are shown in Fig. 2-23. The crack growth rate has been computed separately for every load block within the demonstrator tests. In Fig. 2-23 the crack growth rate has been normlized with respect to the CA baseline value, i.e. the value obtained from Paris law in Eq. 2-7. Hence, a value of $da/dN_{VA} \,/\, da/dN_{CA} = 1$ corresponds to a crack growth rate equal to the CA baseline response. Certain load blocks have a short duration, which makes the computation of the crack growth rate less convenient.

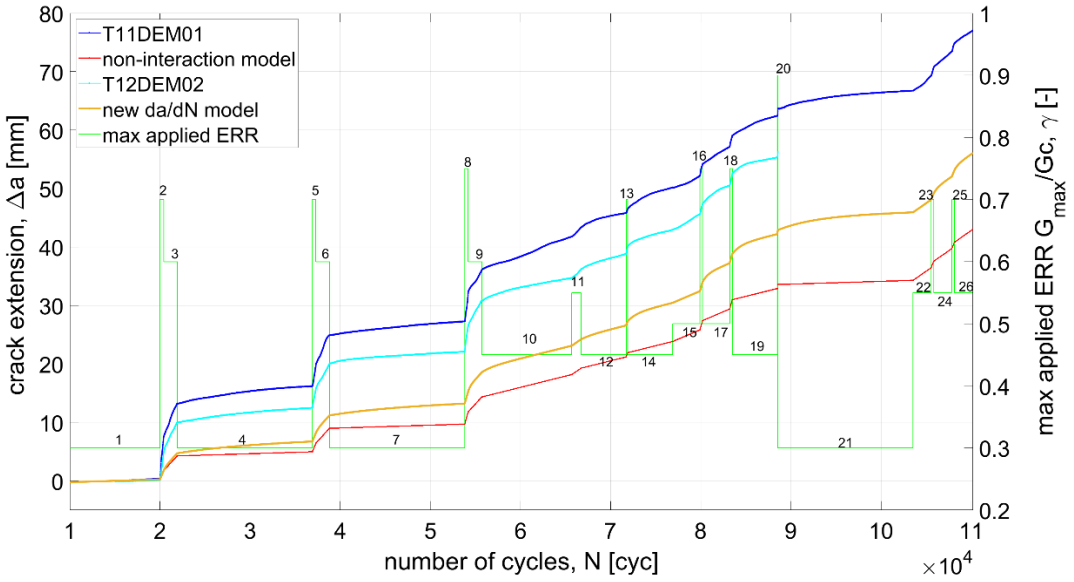

Figure 2-22: Left axis: Crack extension, $\boldsymbol{\Delta a}$, versus the number of load cycles in the demonstrator test. Right axis: The maximum applied ERR (target) normalized with respect to the materials fracture toughness.

Generally, the crack growth rate is higher during the VA test in comparison to the CA baseline. In several of the L-load blocks the crack growth rate is more than a factor of 5 times the crack growth rate at CA baseline. The demonstrator tests show the characteristic exponential decay-type behaviour at several HL load amplitude changes, which is similar to the trend observed in the two-level block amplitude loading tests. Additionally, Fig. 2-23 shows that the crack growth rate following a HL-load amplitude change increases as the magnitude of the step change in ΔG_{max} increases, which was also observed in the BL tests in Fig. 2-20. The crack extension, Δa, and the crack growth rate, da/dN, in the demonstrator tests are analysed further by comparison with the conventional non-interaction model and the new crack growth rate model. The predictions made from the concentional non-interaction model and the new crack growth rate model are shown by the red graph and yellow graph, respectively.

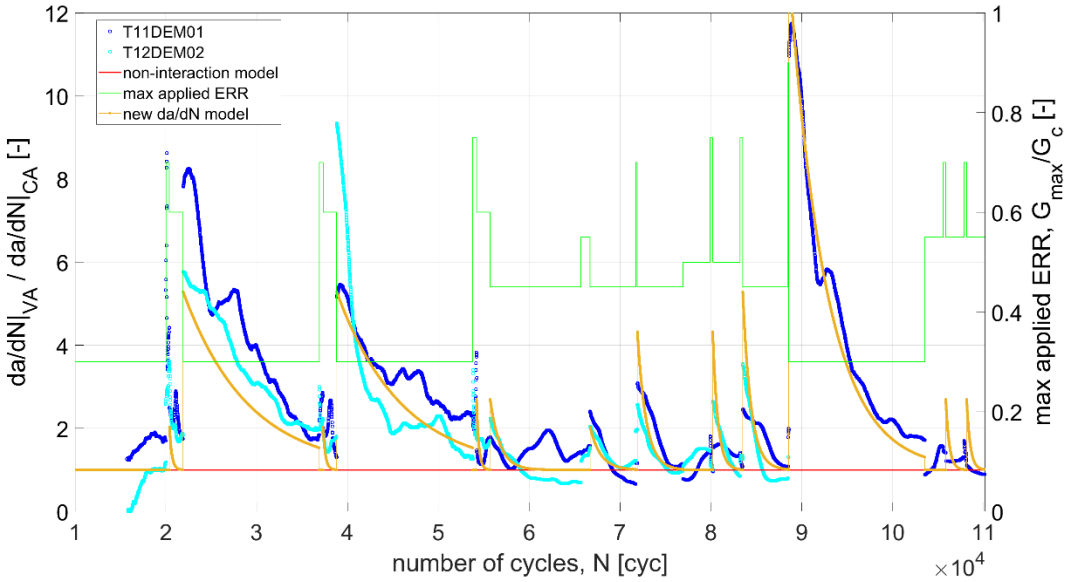

Figure 2-23: Left axis: The crack growth rate versus the number of load cycles in the VA demonstrator test. The measured crack growth rate, da/dN_{VA}, has been normalized with respect to the CA baseline crack growth rate, da/dN_{CA}, as obtained by Paris law. Right axis: The maximum applied ERR (target) normalized with respect to the materials fracture toughness.

A simple one-dimensional crack growth prediction is computed using the new crack growth rate model and an incremental procedure with numerical integration of the rate equation by a trapezoidal integration rule. The crack growth prediction is included in Fig. 2-23. The interaction model computes a total crack extension after $N_{tot} = 110{,}150$ load cycles of $\Delta a_{pred} = 60.69$ mm in comparison to the crack extension $\Delta a_{exp} = 77.07$ mm measured in the experiment *T11DEM01*. This gives an average error of $\Delta a_{exp}/\Delta a_{pred} = 1.27$ for the entire load spectrum, which is still noticeable, however, an improvement in comparison to the error of the non-interaction model for which $\Delta a_{exp}/\Delta a_{pred} = 1.65$. The load block numbers 3, 6, 13, 16, 18, 20 show a significant reduction of the model error. In certain load blocks, the relative error in the crack extension with respect to the non-interaction model is reduced from more the 200-300 % to less than 10%-50% within a given load block number. An error of the interaction model is still present and expected as the experimentally observed high crack growth rates following LH load amplitude changes have not been included in the model. A noticeable error occurs in the prediction from the new crack growth rate model in Fig. 3 because a large amount of crack extension occurs during the initial load blocks (no. 2-3, 5-6, and 8-9) that have character of being H-load blocks. However, the increased crack growth rate following LH load amplitude changes are shown to reduce as the number of load amplitude changes increases – like the tendency observed in Fig. 2-18(a),(c) and Fig. 2-19(a),(c). The interaction model provides a good representation of the crack growth rate following the HL load amplitude changes in the multi-level block loading tests (cf. Fig. 4). The transient crack growth rates following the HL load amplitude changes are well-captured with respect to the amount of overshoot and the duration of rate of decay of the transient responses. The new crack growth rate model provides a good representation of the crack growth rate following the HL load amplitude changes in Fig. 2-24. The transient crack growth rates following the HL load amplitude changes are well-captured with respect to the amount of overshoot and the duration of rate of decay of the transient responses.

3. Finite element simulations

3.1. Transient behaviour

In order to take the transient effects into account, the method divides each load block into two sub-blocks: A transient phase (in orange in Figure 3-1) and a steady-state phase (in green in Figure 3-1). If the load block ends before the steady-state phase is reached, then only the transient phase is present (see, for example, the load block from N_1 to N_2 in Figure 3-1).

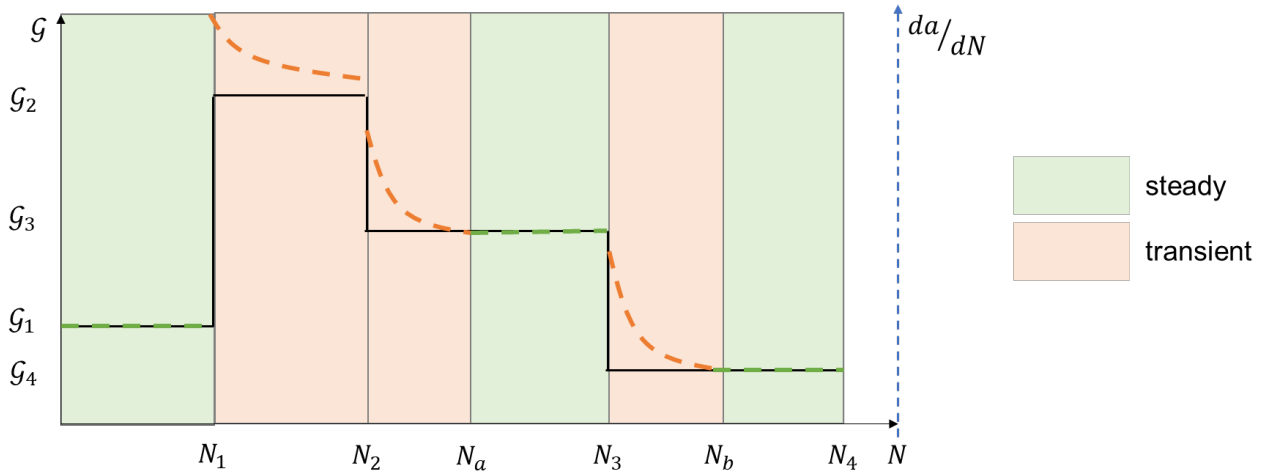

Figure 3-1. Transient and steady state behaviours during a sequence of load blocks.

During the steady-state phases, the crack growth rate follows the Paris' law-like relation:

$$\frac{da}{dN} = A\left(\frac{\mathcal{G}_{max}\,(1-R)}{\mathcal{G}_c}\right)^p \qquad \text{Eq. 3-1}$$

where A and p are the Paris' law parameters, $\mathcal{G}$ is the maximum cyclic energy release rate, $\mathcal{G}_c$ is the fracture toughness, R is the load ratio.

During the transient phases an additional crack growth rate term is added to the Paris' law relation following an exponential decay function:

$$\frac{da}{dN} = A\left(\frac{\mathcal{G}_{max}\,(1-R)}{\mathcal{G}_c}\right)^p \left(1 + \bar{B}e^{-\bar{m}(N-N_0)}\right) \qquad \text{Eq. 3-2}$$

where $\bar{B}$ and $\bar{m}$ are the exponential decay function parameters, N is the number of cycles and N_0 is the number of cycles at which the current load block begins. The number of cycles at which the transient sub-block ends is determined solving the exponential decay function for a crack growth rate, da/dN, close to that corresponding to the steady-state value. For instance, if the transient phase is assumed to terminate when the crack growth rate is 1.01 times the steady-state value (Paris' law value), then the duration of the transient phase can be determined by solving the following equation for N:

$$\frac{da}{dN} = 1.01\frac{da}{dN_{ss}} \Leftrightarrow$$

$$A\left(\frac{\mathcal{G}_{max}\,(1-R)}{\mathcal{G}_c}\right)^p \left(1+\bar{B}e^{-\bar{m}(N-N_0)}\right) = 1.01\,A\left(\frac{\mathcal{G}\,(1-R)}{\mathcal{G}_c}\right)^p$$

Or equivalently:

$$\bar{B}e^{-\bar{m}(N-N_0)} = 0.01 \Leftrightarrow$$

$$N - N_0 = \frac{1}{\bar{m}}\ln\left(\frac{\bar{B}}{0.01}\right)$$

Eq. 3-3

If the value of $N - N_0$ is larger than the duration of the current load block, then the steady-state phase is not reached before the next load amplitude change and only a transient behaviour is observed (see, for example, the load block from N_1 to N_2 in Figure 3-1). However, if the value $N - N_0$ is smaller than the duration of the load block, the transient behaviour ends at N load cycles and steady-state behaviour is observed during the remaining cycles of the load block. For example, in Figure 3-1, the load block from N_2 to N_3 is divided into two sub-blocks: The transient behaviour (from N_2 to N_a) and the steady-state behaviour (from N_a to N_3). Thus, Eq. 3-3 is fulfilled for $N = N_a$.

3.2. Cycle jump strategy

The cycle jump is based on a user-defined target crack length increment, Δa_t. For a sub-block with steady-state crack growth behaviour, the crack length increment over a cycle jump from N_{i-1} to N_i is:

$$\Delta a_t = A\left(\frac{\mathcal{G}\,(1-R)}{\mathcal{G}_c}\right)^p (N_i - N_{i-1})$$

Eq. 3-4

Where the variables N_{i-1} and N_i is the number of load cycles at the last converged increment and at the current time increment after the cycle jump, respectively. For a sub-block with transient crack growth behaviour, the crack length increment over a cycle jump is found by integration of Eq. 3-2:

$$\Delta a_t = \left(\frac{\bar{B}}{m}\left(e^{-m\,(N_{i-1}-N_0)} - e^{-m\,(N_i-N_0)}\right) + (N_i - N_{i-1})\right) A(\mathcal{G}_{max})^p$$

Eq. 3-5

Thus, by solving Eq. 3-5 for N_i, the number of cycles at which the crack will have propagated a distance Δa_t is:

$$N_i = \frac{-\bar{B}e^{-m\,N_{i-1}} + \Delta a_t\,m + bmN_{i-1} + b\,W\left(e^{\left(m\left(-\Delta a_t - bN_{i-1} + e^{(-mN_{i-1})\bar{B}/m}\right)\right)/b\,\frac{\bar{B}}{b}}\right)}{b\,m}$$

Eq. 3-6

Where $b = A(\mathcal{G}_{max})^p$ and $W(z)$ is the Lambert function. In the implementation of this method into finite elements, $W(z)$ is approximately solved [39] as:

$$W(z) \sim \frac{2\ln(1+By) - \ln(1+C(\ln(1+Dy)) + E}{1 + \frac{1}{2\ln(1+By) + 2A}} \quad \text{Eq. 3-7}$$

Where $A = 2.344, B = 0.8842, C = 0.9294, D = 0.5106, E = -1.213$ and $y^2 = 2ez + 2$.

3.3. Exponential decay function parameters

In this model, it is assumed that the parameters of the exponential decay function, $\bar{B}$ and $\bar{m}$, are function of the increment in ERR, G, between subsequent load blocks, $\Delta\mathcal{G}$. Two interpolations are suggested:

- One for the transition from a high load block to a low load block (HL):

$$\bar{m}^{HL} = {m_3}^{HL}\left(\frac{\Delta\mathcal{G}}{\mathcal{G}_c}\right)^3 + {m_2}^{HL}\left(\frac{\Delta\mathcal{G}}{\mathcal{G}_c}\right)^2 + {m_1}^{HL}\frac{\Delta\mathcal{G}}{\mathcal{G}_c} + {m_0}^{HL}$$
$$\bar{B}^{HL} = {B_3}^{HL}\left(\frac{\Delta\mathcal{G}}{\mathcal{G}_c}\right)^3 + {B_2}^{HL}\left(\frac{\Delta\mathcal{G}}{\mathcal{G}_c}\right)^2 + {B_1}^{HL}\frac{\Delta\mathcal{G}}{\mathcal{G}_c} + {B_0}^{HL} \quad \text{Eq. 3-8}$$

- And another for the transition from a low load block to a high load block (LH):

$$\bar{m}^{LH} = {m_3}^{LH}\left(\frac{\Delta\mathcal{G}}{\mathcal{G}_c}\right)^3 + {m_2}^{LH}\left(\frac{\Delta\mathcal{G}}{\mathcal{G}_c}\right)^2 + {m_1}^{LH}\frac{\Delta\mathcal{G}}{\mathcal{G}_c} + {m_0}^{LH}$$
$$\bar{B}^{LH} = {B_3}^{LH}\left(\frac{\Delta\mathcal{G}}{\mathcal{G}_c}\right)^3 + {B_2}^{LH}\left(\frac{\Delta\mathcal{G}}{\mathcal{G}_c}\right)^2 + {B_1}^{LH}\frac{\Delta\mathcal{G}}{\mathcal{G}_c} + {B_0}^{LH} \quad \text{Eq. 3-9}$$

4. Implementation into SAMCEF software

4.1. Numerical verification example

The transient effect described in the previous sections was implemented in Simcenter Samcef solver v2206 for both behaviour FATINT and FATINT2 (interlaminar fatigue damage model respectively uncouple and couple with intralaminar fatigue damage). The material defining in the Samcef deck are:

.MAT I material_number

NOM "material_name"

BEHA "FATINT"or "FATINT2" Behavior selection

CFAT m_{0HL} m_{0LH} NF *nfmhl nfmlh*

$$m^{\mathrm{HL}} = m_{0HL}.f_{nfmhl}\left(\frac{|\Delta\mathcal{G}|}{\mathcal{G}_c}\right)$$

$$m^{LH} = m_{0LH}.f_{nfmlh}\left(\frac{|\Delta\mathcal{G}|}{\mathcal{G}_c}\right)$$

BIGB b_{0HL} b_{0LH} NF *nfbhl nfblh*

$$B^{\mathrm{HL}} = b_{0HL}f_{nfbhl}\left(\frac{|\Delta\mathcal{G}|}{\mathcal{G}_c}\right)$$

$$B^{LH} = b_{0LH}f_{nfblh}\left(\frac{|\Delta\mathcal{G}|}{\mathcal{G}_c}\right)$$

The polynomial function proposed in Eq. 3-8 and Eq. 3-9 can be defined via .FCT command with the associated function number, nfi (i={mhl,mlh,bhl,blh}).

The block of loadings are defined by pair of subcases: One without the fatigue cycle jump algorithm to apply the load amplitude change and another one to apply the fatigue analysis. The transient behaviour is deactivated if b0HL = 0 or if the subcase number is inferior or equal to two (no transient effect at the first block cycle).

4.2. Numerical verification examples

This section offers two examples that serve to verify the implementation into the FE formulation. Both examples are DCB tests under fatigue loading. The DCB specimens have a $[0°]_6$ stacking sequence. The dimensions of the specimen and the FE model are illustrated in Figure 4-2. The properties of the bulk material are listed in Table 4-2. Only the middle of the specimen is simulated with one layer in the transversal direction using a plane strain condition, which corresponds to the behaviour of the mid-width of the specimen. The moment loading is applied via shell element with elastic steel properties glued to the solid element via node to edge conditions. The boundaries conditions are the following:

- All nodes are fixed according to the transverse direction for plane strain state
- All nodes at X=L are fixed on longitudinal and thickness direction
- Moment applied at end of shell element with a loading ratio R
- Initial crack: set Damage = 1 for cohesive element where X < a_0

Notice the verification examples in Sec. 4.2.1 uses a slightly different version of Eq. 3-2 as shown by Eq. 3-2* here:

$$\frac{da}{dN} = A\left(\frac{\mathcal{G}_{max}\,(1-R)}{\mathcal{G}_c}\right)^p + \bar{B}e^{-\bar{m}(N-N_0)}$$	Eq. 3-2*

The specific parameters used in the verification examples are provided in Sec. 4.2.1. The same procedure has been applied to verify the FE implementation of Eq. 3-2, however, the results are not presented in this report. The demonstrator test in Sec. 4.2.2 uses the version in Eq. 3-2.

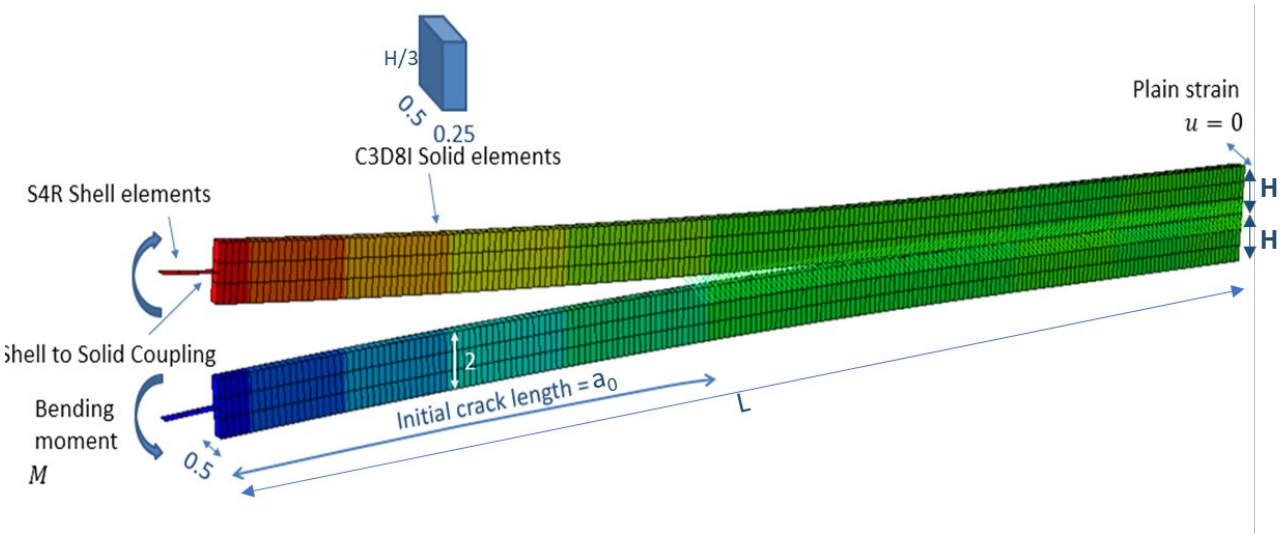

Figure 4-1. Characteristics of the DCB model.

E11: Longitudinal Young's modulus	37.2E3
E22: Transversal Young's modulus	15.08E3
E33: Transversal Young's modulus	14.2E3
nu12: Poisson's coefficient in the longitudinal planes	0.308
nu13: Poisson's coefficient in the longitudinal planes	0.25
nu23: Poisson's coefficient in the transversal plane	0.33
G12: Shear modulus in the longitudinal planes	4.828E3
G12=G13: Shear modulus in the longitudinal planes	2.2E3
G23: Shear modulus in the transversal plane	1.5E3

Table 4-1. Properties of the bulk material.

4.2.1 Numerical validations

The first analysis was developed to validate the method and validated via expected analysis values. The analysis was performed in a first step with the Abaqus solver with the method were developed and then with the Samcef solver to validate its implementation.

The dimension of the specimen is:

H	3*1.357 mm
L	50 mm
a0	20 mm

Table 4-2. Geometric parameters for the DCB numerical validation

Eight steps are defined:

- A quasi-static ramp from unloaded to a prescribed moment of 180 (90 x 2 nodes).
- A fatigue step at constant maximum cyclic moment of 180 during 300 cycles.
- A quasi-static ramp from unloaded to a prescribed moment of 140 (70 x 2 nodes).
- A fatigue step at constant maximum cyclic moment of 140 during 5000 cycles.
- A quasi-static ramp from unloaded to a prescribed moment of 160 (80 x 2 nodes).
- A fatigue step at constant maximum cyclic moment of 160 during 500 cycles.
- A quasi-static ramp from unloaded to a prescribed moment of 130 (65 x 2 nodes).
- A fatigue step at constant maximum cyclic moment of 130 during 20000 cycles.

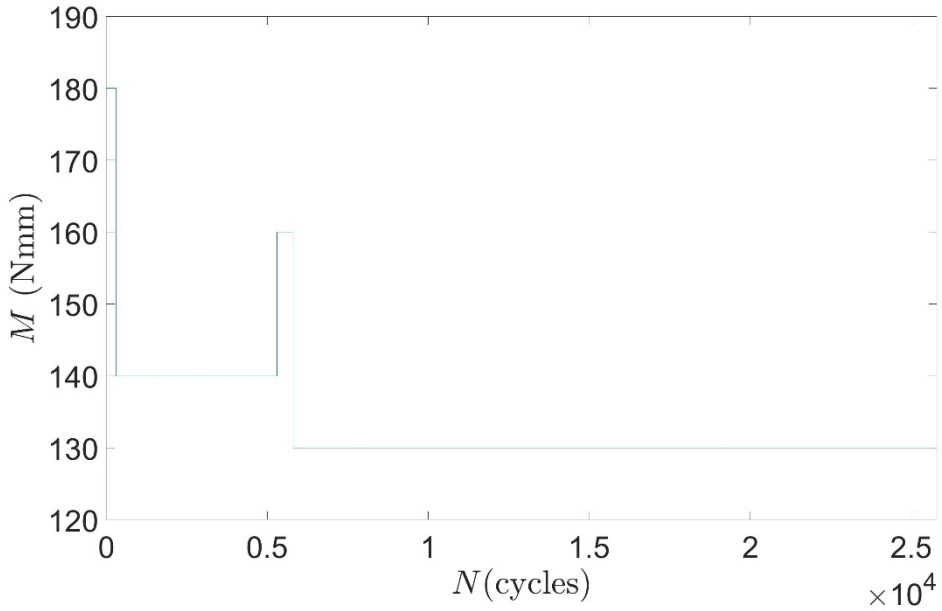

Figure 4-2. Evolution of the applied moment as a function of the number of cycles

The input parameters of the cohesive elements are provided Tab. 4-3.

GIc	1.359
$GIIc$	5.328
$tauIo$	20
$tauIIo$	40

$etaBK$	2
$AParisI$	0.1343
$AParisII$	1
$AParism$	1
$pParisI$	3.984
$pParisII$	1
$pParism$	1
Gth	0
R	0.1
$penstiff$	1E5
$DeltaNuser$	50
$Deltaa$	0.125
$m0\_transHL$	0.00063
$m1\_transHL$	0
$m2\_transHL$	0
$m3\_transHL$	0
$B0\_transHL$	0.00072
$B1\_transHL$	0
$B2\_transHL$	0
$B3\_transHL$	0
$m0\_transLH$	0.00063
$m1\_transLH$	0
$m2\_transLH$	0
$m3\_transLH$	0
$B0\_transLH$	0.00072
$B1\_transLH$	0
$B2\_transLH$	0
$B3\_transLH$	0
my	2E-20
$NLGEOM$	1
$nItetangent$	15

$dama$	0
$ModifiedEstifflag$	1
$correctionSchemeFlag$	1
$surroundingsFlag$	1
$actprint$	1
$Nblocks$	4
$BlockCycles1$	300
$BlockCycles2$	5000
$BlockCycles3$	500
$BlockCycles4$	20000
Other $BlockCycles1$	0
$Transient\_effect$	1

Table 4-3. Input parameters of the cohesive elements used in the DCB case study.

The evolution of the ERR (computed using the J-integral subroutine with Abaqus) as a function of the number of cycles is plotted in Figure 4-3.

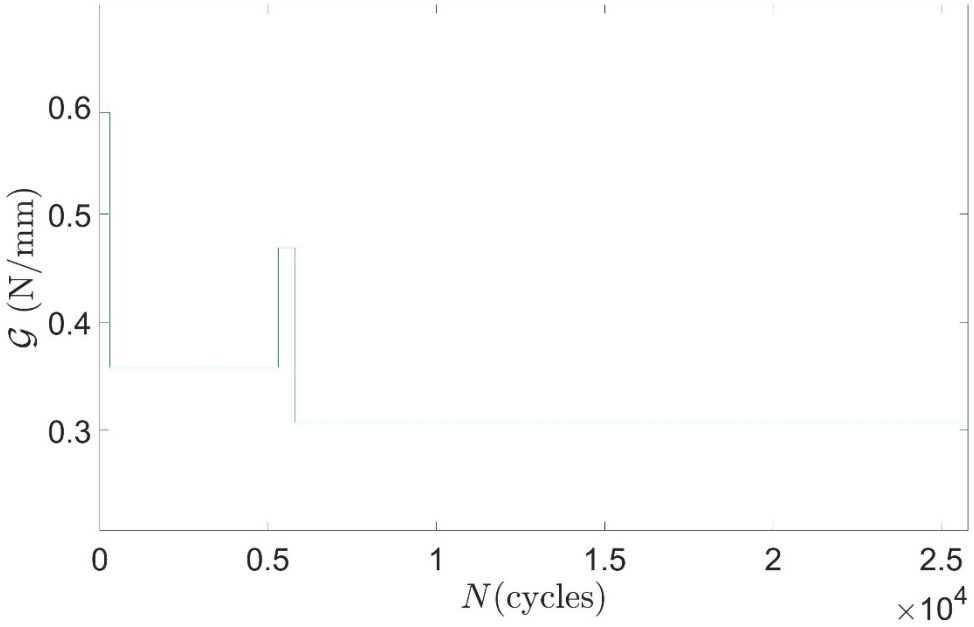

Figure 4-1. Evolution of the energy release rate as a function of the number of cycles with Abaqus.

Figure 4-4 to Figure 4-7 show the evolution of the crack length increment during the fatigue steps. A user-defined fitting of the $\Delta a(N - N_0)$ output data has been done using Eq. 3-5.

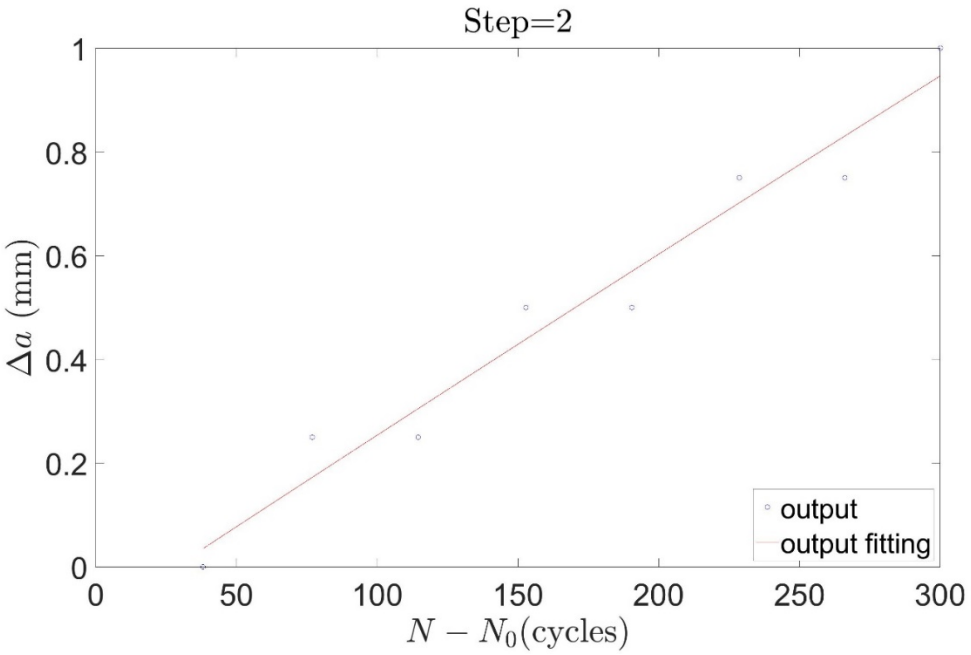

Figure 4-2. Evolution of the crack length increment as a function of the number of cycles during step 2 with Abaqus.

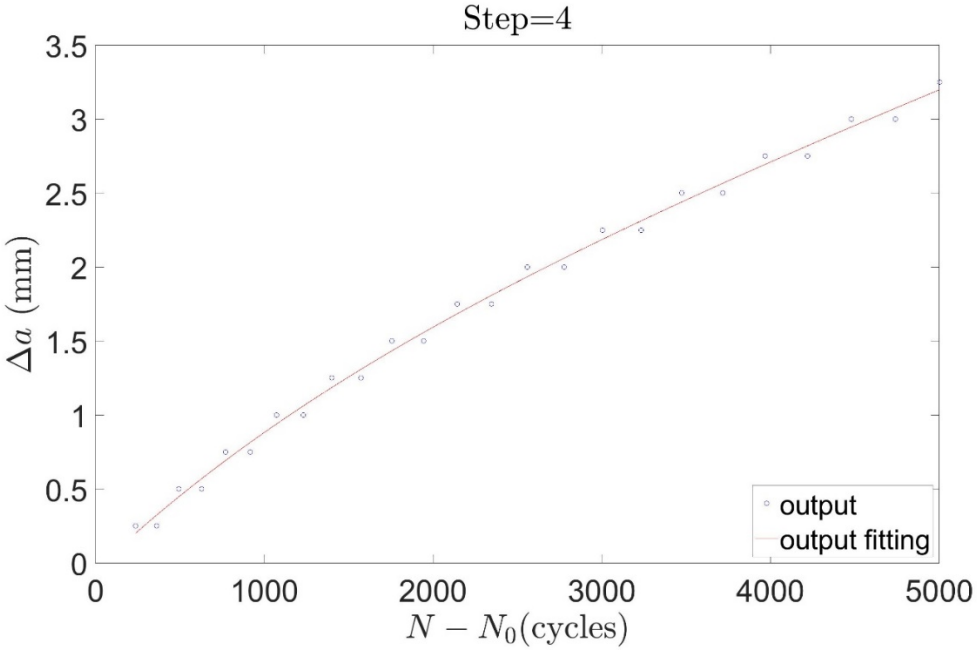

Figure 4-3. Evolution of the crack length increment as a function of the number of cycles during step 4 with Abaqus.

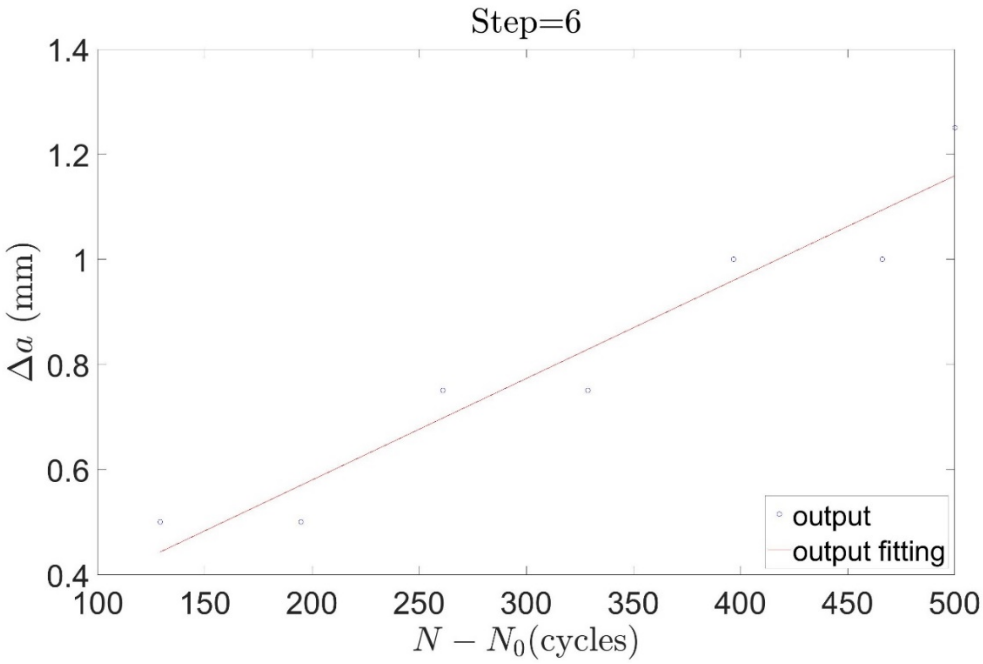

Figure 4-4. Evolution of the crack length increment as a function of the number of cycles during step 6 with Abaqus.

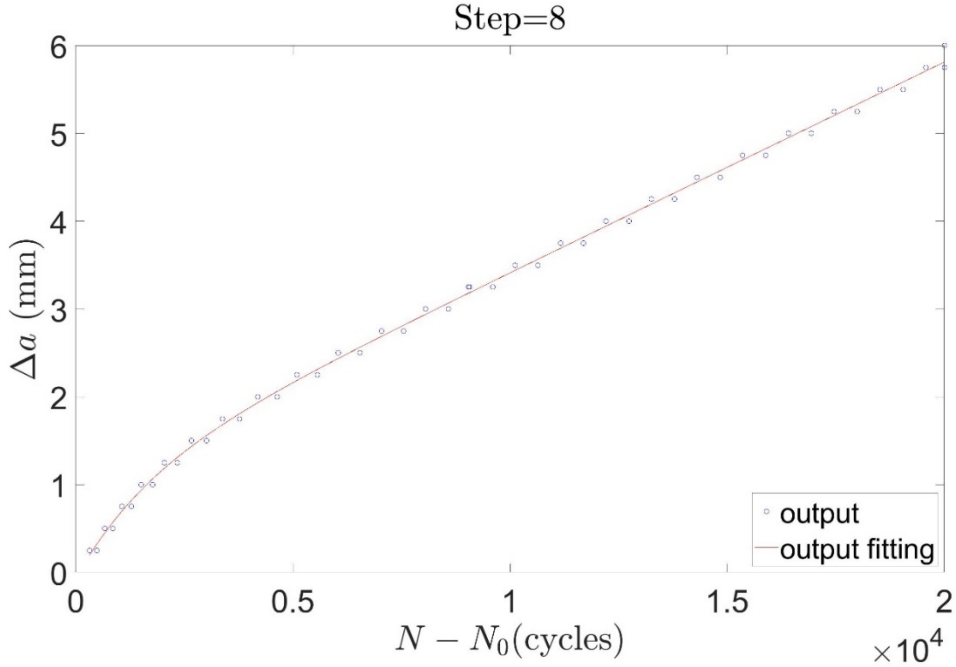

Figure 4-5. Evolution of the crack length increment as a function of the number of cycles during step 8 with Abaqus.

Figure 4-8 to Figure 4-11 show the evolution of the crack growth rate during the fatigue steps. The exponential decay function input to the model following Eq. 3-2 are compared to the derivative of the expression fitting the crack length increment shown in Figure 4-4 to Figure 4-7.

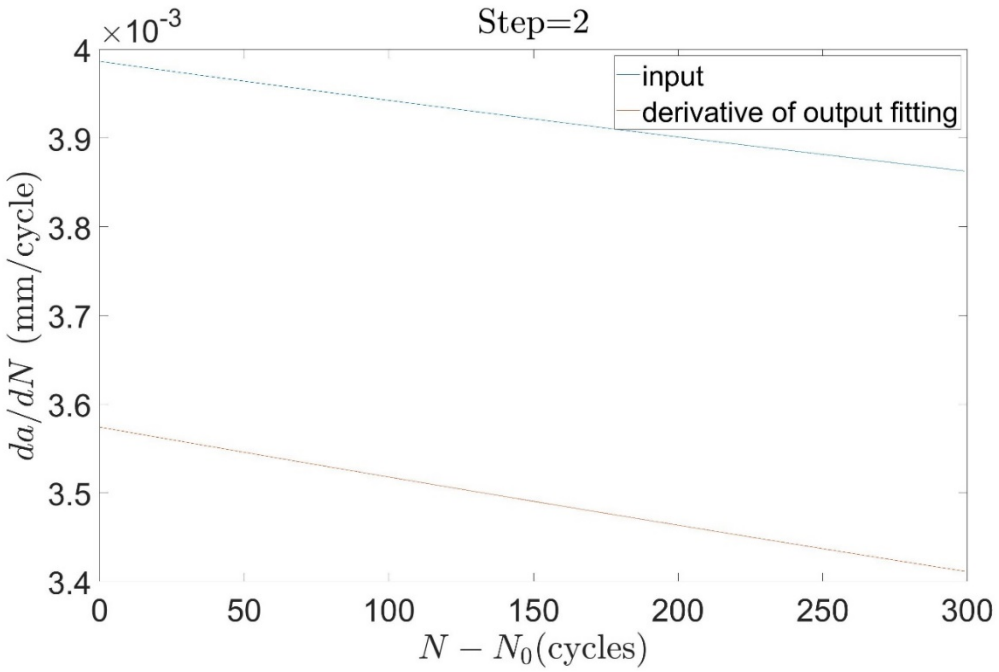

Figure 4-6. Evolution of the crack growth rate as a function of the number of cycles during step 2 with Abaqus.

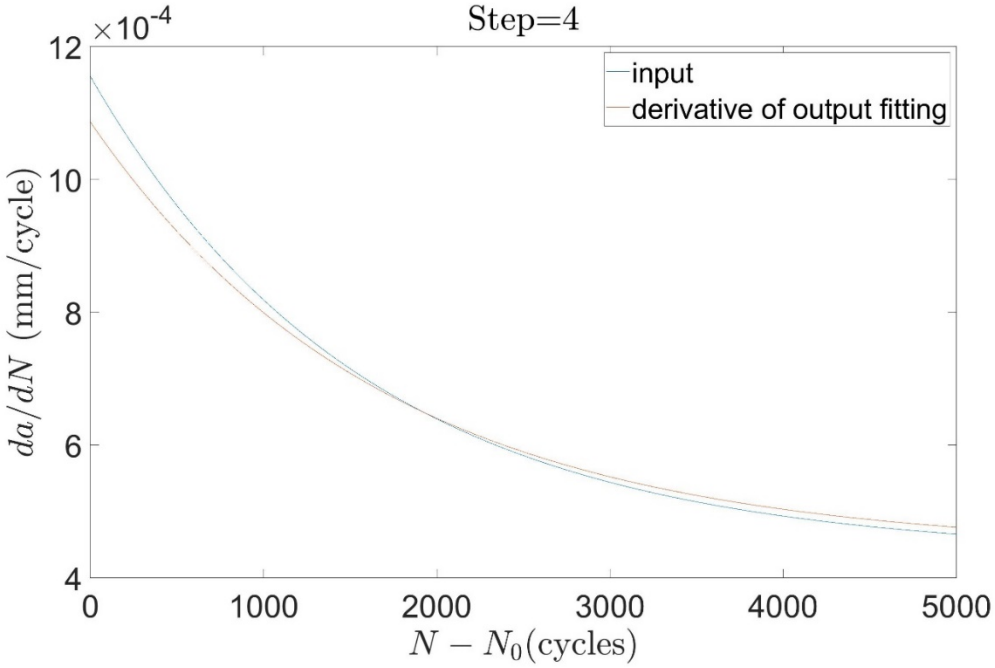

Figure 4-7. Evolution of the crack growth rate as a function of the number of cycles during step 4 with Abaqus.

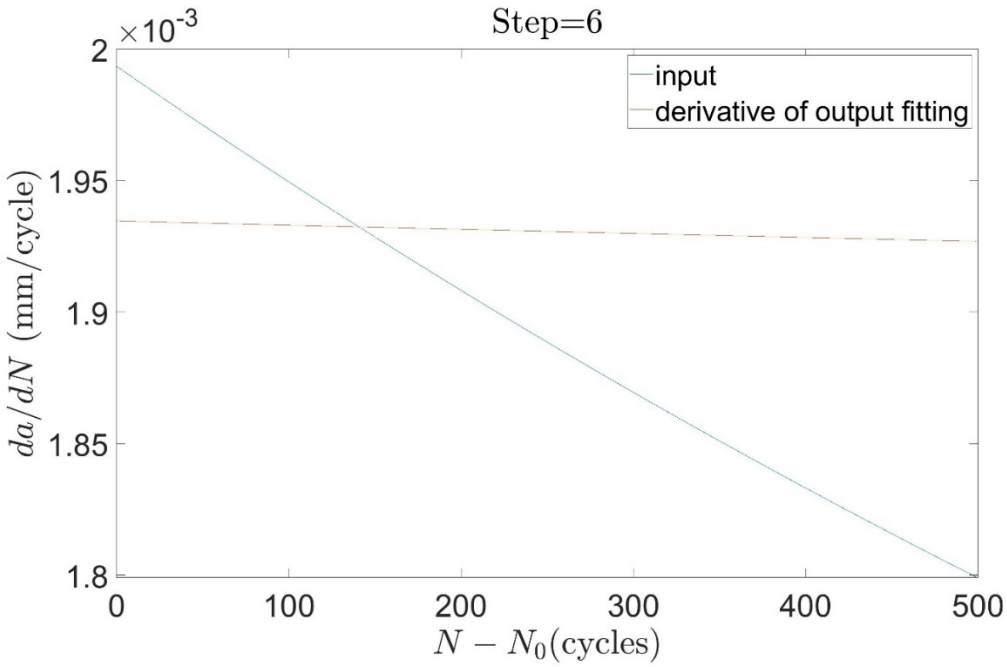

Figure 4-8. Evolution of the crack growth rate as a function of the number of cycles during step 6 with Abaqus.

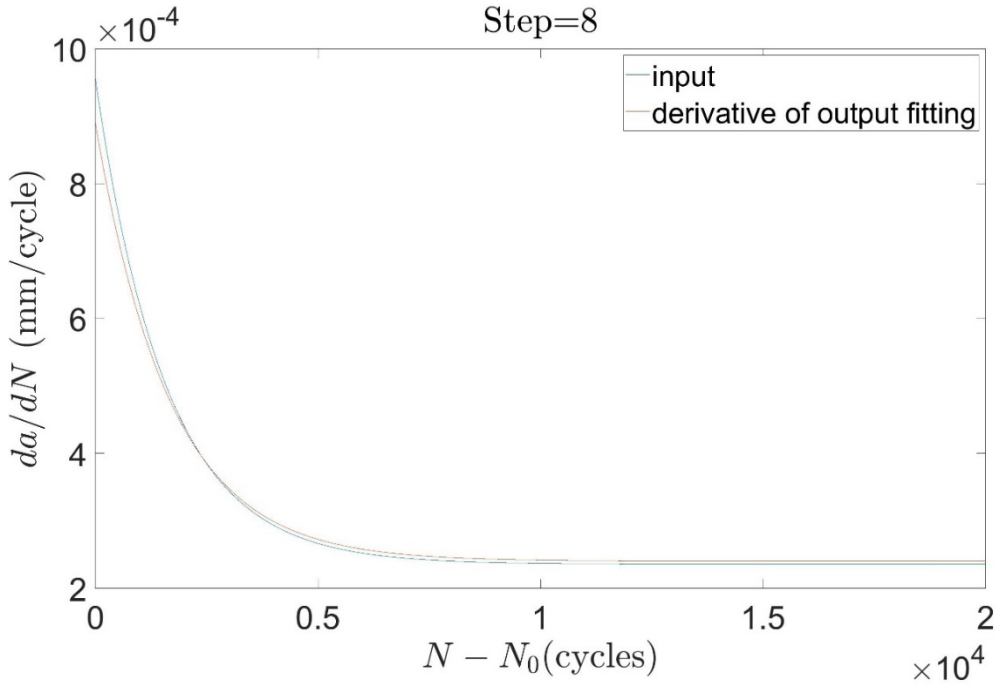

Figure 4-9. Evolution of the crack growth rate as a function of the number of cycles during step 8 with Abaqus.

Table 4-3 compares the input crack growth rate decay function and the fitting of the behaviour obtained from simulations.

Input	Derivative of the fitting of the $\Delta a(N - N_0)$ output
$\frac{da}{dN} = 0.0033 + 0.00072e^{0.00063\ (N-N_0)}$	$\frac{da}{dN} = 0.001941 + 0.001637e^{0.0003653\ (N-N_0)}$
$\frac{da}{dN} = 0.0004 + 0.00072e^{0.00063\ (N-N_0)}$	$\frac{da}{dN} = 0.0004423 + 0.0006438e^{0.0005906\ (N-N_0)}$
$\frac{da}{dN} = 0.0013 + 0.00072e^{0.00063\ (N-N_0)}$	$\frac{da}{dN} = 0.001827 + 0.0001065e^{0.0001243\ (N-N_0)}$
$\frac{da}{dN} = 0.0002 + 0.00072e^{0.00063\ (N-N_0)}$	$\frac{da}{dN} = 0.0002399 + 0.0006497e^{0.0005995\ (N-N_0)}$

Table 4-4. Comparison between the input crack growth rate decay function and the derivative of the fitting of the crack length extension.

The simulation were reproduced with the Samcef solver. An Octave script were developed in order to plot the evolution of the crack length, $\Delta a = f(N - N0)$ for each load block. It consists to output via Samcef postprocessing module, ***Baconpost***, to output in a ASCII file the nodal based energy damage for all cohesive nodes at each time step. With the initial longitudinal nodal position, a plot of $De = f(X)$ is generated and then the crack position is defined at the maximal X position where De is non-zero. This enables to compute the crack increment Δa at each saved time step.

The simulation is run excluding the load history effect to validate the model and including the load history effect. Fig. 4-13 and Fig. 4-14 show the results with and without the load history effect, respectively. The figures include the Samcef results in comparison to the crack increment prediction obtained from the Octave script (i.e. the expected results).

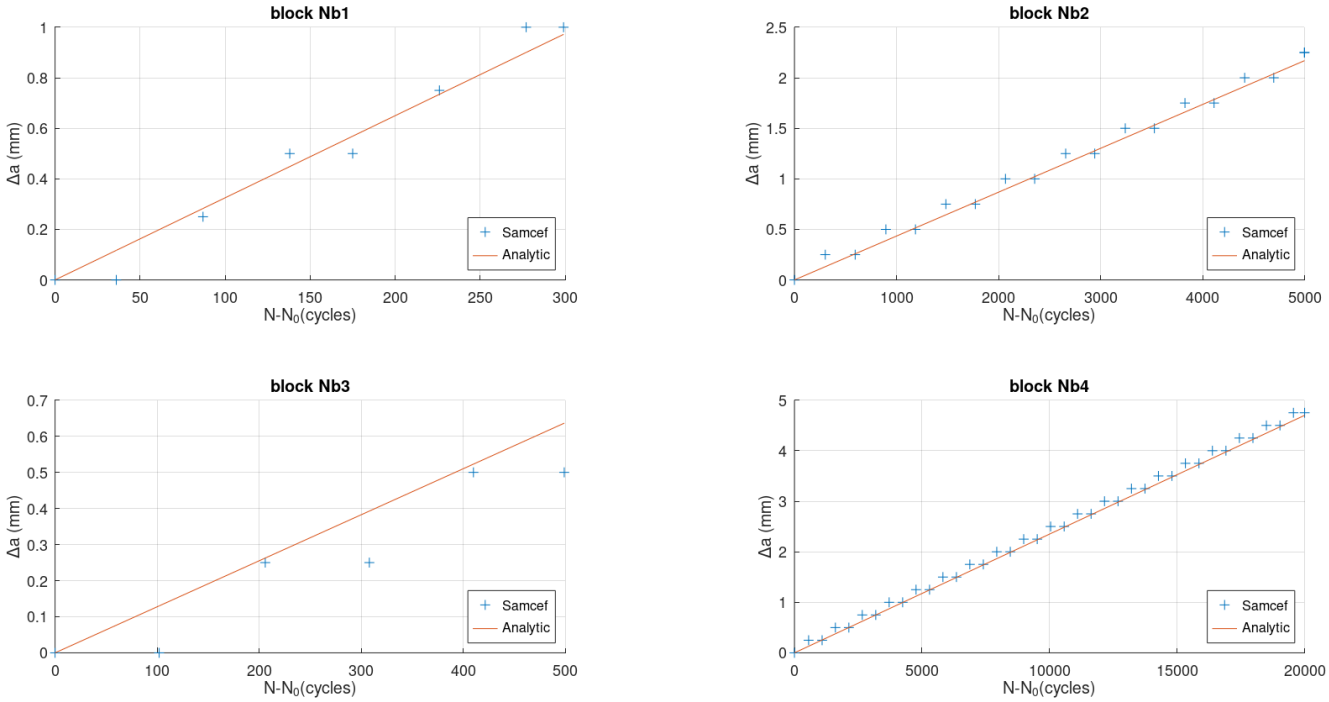

Figure 4-10. Evolution of crack growth length for each block without historical load effect simulation via Samcef and analytically with Samcef

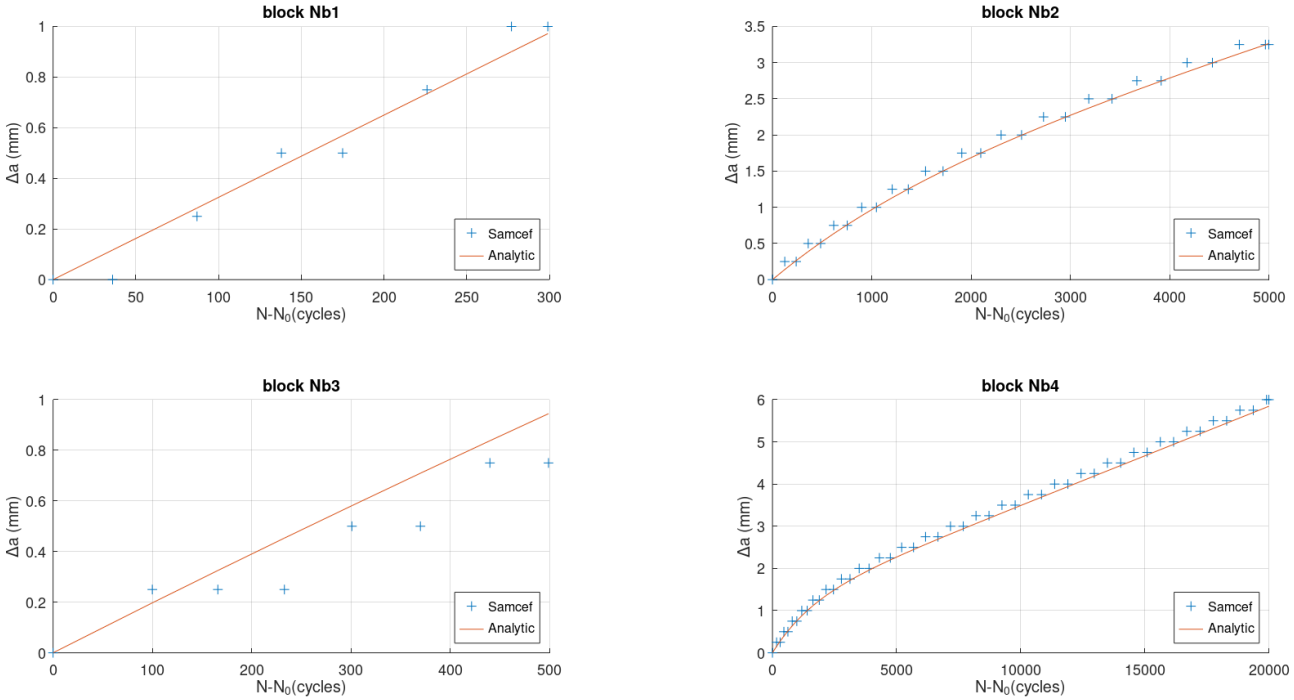

Figure 4-11. Evolution of crack growth length for each block with historical load effect simulation via Samcef and analytically with Samcef

4.2.2 Demonstrator VA test

The same FE methods were applied to simulate the multi-level block loading test presented in Sec. 2.

H	4.1 mm
L	657 mm
a0	100 mm
w	27.8 mm

Table 4-5. Geometric parameters for the DCB numerical validation

The input parameters for the cohesive element are:

GIc	1.359
$GIIc$	5.328
$tauIo$	20
$tauIIo$	40
$etaBK$	2
$AParisI$	0.0727
$AParisII$	1
$AParism$	1
$pParisI$	5.13
$pParisII$	1
$pParism$	1
Gth	0
R	0.2
$penstiff$	1E5
$DeltaNuser$	50
$Deltaa$	0.125
$m0\_transHL$	-5.77E-5
$m1\_transHL$	-2.771E-4
$m2\_transHL$	0
$m3\_transHL$	0
$B0\_transHL$	0
$B1\_transHL$	6.43
$B2\_transHL$	20.99

B3_transHL	0
m0_transLH	0
m1_transLH	0
m2_transLH	0
m3_transLH	0
B0_transLH	0
B1_transLH	0
B2_transLH	0
B3_transLH	0

Table 4-6. Input parameters of the cohesive elements used in the Demonstrator VA test case study.

The simulation was performed with the Samcef solver. A Python script were developed to plot the evolution of the crack length, $\Delta a = f(N)$. It consists two output via Samcef postprocessing module, ***Baconpost***, to output in an ASCII files the nodal based energy damage, De, for all cohesive nodes at each time step. With the initial longitudinal nodal position, X, a plot of $De = f(X)$ is generated and then the crack position is defined at the maximal X position where De is not null. This enables to compute Δa at each saved time step. Another one equivalent method were applied to pick the maximum crack release energy $Gmax$ in the model were $Gmax = max(G(X))$.

Fig. 4-14 presents the evolution of the crack extension and the maximum applied ERR with the number of the cycles. The FE model fails to converge after load block number 20. Time allowing, both the convergence issue would have been solved and the graph in Fig. 4-14 updated. Nevertheless, the graph show a significant improvement in the crack length prediction in comparison to the conventional non-interaction model prediction.

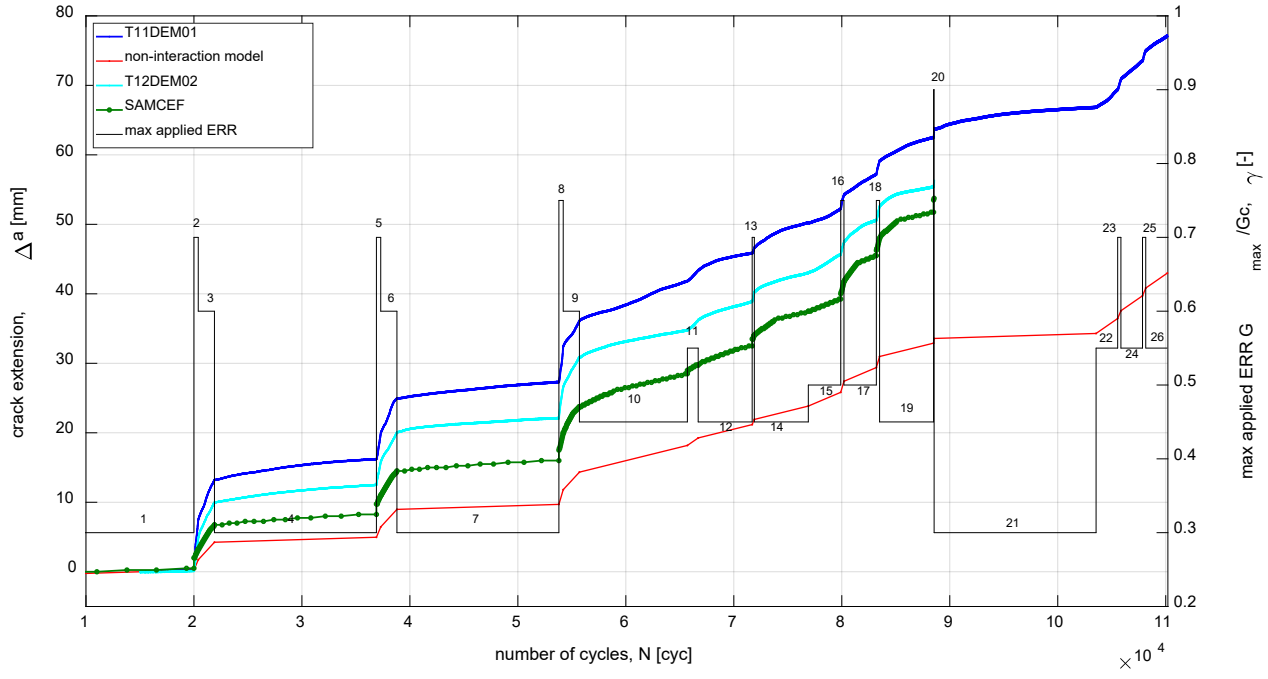

Figure 4-12 : Evolution of ERR and crack extension in VA demonstrator simulation

5. Intra-laminar VA tests

5.1. Introduction

The focus now shifts to the effect of load history on the evolution of intralaminar damage under flexural fatigue loading. The work takes point of departure in the recent experimental work by *Bender et al*. [27]. The authors in [27] monitored the evolution of the intralaminar damage state by measuring crack accumulation and growth in the 0° mid-layer of multidirectional ($[\pm 45/0_5]_S$), waisted coupons subjected to tension-tension fatigue with CA and VA loading. Their test setup consisted of white light transmitted through the specimen to reveal intralaminar microcracks and a high-definition camera trained on the centre of the gauge section using a telephoto lens to achieve a high-magnification factor. Adding in complexity was the need for extensive image treatment and processing via the development of sophisticated image processing and computational scripts. The work provides important findings on intralaminar crack initiation and propagation during two-level block loading to explain the damaging effect of the so-called cycle-mix effect. As part of Task 5-4 of this project, SINTEF performed a targeted test campaign inspired by the experimental work of Bender *et al*. [27] on intralaminar crack initiation and propagation during VA block loading, while devising a simpler test configuration and damage state monitoring method that can be readily implemented by most any research group with access to a universal fatigue testing machine. Only a few research groups globally possess the setup and competence to perform *in situ* crack density monitoring, e.g. [40, 32, 41, 27, 42], one such group being the *CraCS Research Group* at Aalborg University in Denmark [27]; other crack counting methods such as [5] and [43] rely instead on interrupted testing and fractography, which is a more conventional method albeit less insightful while equally painstaking.

The present investigation experimentally looks at whether the transition from VA-H to VA-L block-loading segments accelerate the damage response in a transverse ($[90]_{2S}$) GFRP laminate as compared to CA-H and CA-L loading alone. This work builds on the CA loading experiments devised and performed in Task 5-2 of this project and detailed in Deliverable Report D5-2 (UPWARDS_D5-2_M24_vF). A one-sided flexural load configuration was selected in Task 5-2 to significantly reduce the quantity and total duration of tests necessary for the reverse estimation of parameters used in a state-of-the-art, interlaminar progressive damage model [44]. Flexural loading remains relevant herein as it simplifies specimen manufacturing and positioning and is more representative of real-world component load cases.

In turn, the key damage mechanisms and interaction thereof have been experimentally established for VA loading of multidirectional laminates, for instance in [5]. The selection of a transverse test direction makes use of the established fact that intralaminar damage initiates in the transverse plies of multidirectional laminates in the form of matrix micro-cracking when subjected to in-plane tension. A simpler damage monitoring approach may then be based on stiffness degradation alone, obtained by tracking the midspan deflection of flexural coupons. This method may prove adequate to observe notable events and state changes during the evolution of intralaminar damage in the form of transitions between increasing rates of stiffness degradation. Events such as through-thickness intralaminar cracks reaching the first tensile ply interface should appear as curve transitions. Such events can finally be used as points of reference to compare VA, CA-H and CA-L loading cases in terms of the number of H-cycles needed to reach a given intralaminar damage state. The following subsections detail the methodology, deferring to Deliverable Report 5-2 where applicable for conciseness, and present the experimental results and concluding remarks, reflecting on the applicability of this approach for model validation.

5.2. Methodology

Experimental setup

The experimental setup relies on Method B of the ISO-14125 standardized test method for quasi-static flexural testing of fibre-reinforced polymers [45], which specifies the coupon and loading geometries for a four-point loading configuration with support points set at one third of the outer support span. It should be noted that no standardized test method currently addresses the fatigue testing of composite laminates in flexure. Fig. 5-1 presents a schematic of a coupon inserted into the four-point flexure fixture. The test direction runs parallel with the global x-axis. The support points are low-friction rollers made of hardened steel to withstand the abrasive nature of GFRP. In turn, the midspan deflection is tracked by a laser triangulation displacement sensor placed under the specimen (Micro-Epsilon optoNCDT 1420-25). The use of a laser as a contactless sensor is preferrable for fatigue testing as it sidesteps the need for fatigue rating and issues of surface wear at the point of contact. In addition, a laser sensor is straightforward to implement, similar to an LVDT, compared to the added complexity of optical systems such as video extensometers. Finally, the fixture is setup in an Instron 8801 hydraulic fatigue testing machine fitted with a 10 kN load-cell and running in displacement control for quasi-static testing and load-control for fatigue testing. Deliverable Report D5-2 can be perused for additional information regarding the physical setup.

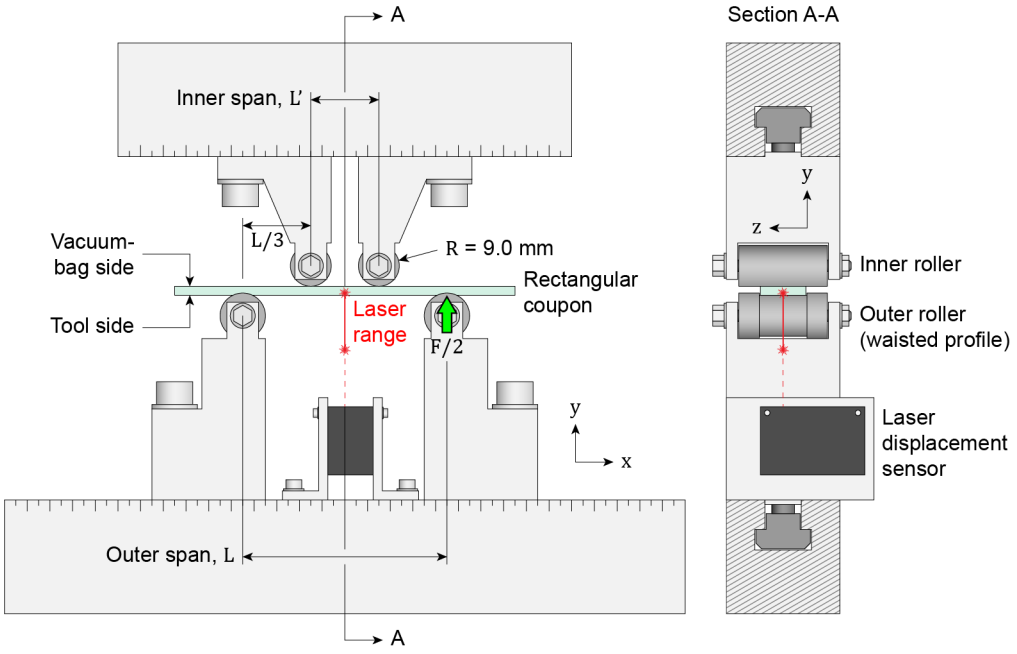

Figure 5-1. Schematic of the four-point flexure test fixture based on ISO-14125 Method B.

Materials

The GFRP laminate was manufactured by Siemens Gamesa Renewable Energy A/S, Denmark. The reinforcement architecture consists of a stacking sequence of unidirectional (UD) non-crimp fabric (NCF) layers that are infused with a toughened epoxy resin via VARTM. The nominal cured ply thickness is approximately 1.0 mm. The coupon and loading geometries are unchanged from Task 5-2 are loosely based on Class III and Annex A of ISO-14125 [45]. The nominal thickness (h), width (b), and length (l) are 4, 20 and 150 mm, respectively. A four-ply stacking sequence of $[0]_{2S}$ is used to achieve the desired thickness, and coupons are cut normal to the fibre orientation to obtain a sequence of $[90]_{2S}$ in the test direction. In turn, the inner (L'/h) and outer (L/h) support span-to-thickness ratios are 7.5 and 22.5, respectively. Finally, coupons are kept in a standard laboratory

environment for at least one week prior to testing (23 ± 2 °C, 50 ± 10% humidity). Deliverable Report D5-2 provides additional details regarding the material and coupon preparation.

Test procedure and program

As in Task 5-2, the stress levels that define the high and low amplitude loading blocks are set as user-defined load fractions, LF, of the A-basis allowable, $\mathrm{T99}$. The latter is a statistical material property calculated from a population of flexural strength (σ_{fB}) measurements. It is used as a conservative strength ceiling such that only 1 in 100 coupons is expected to fail under quasi-static loading. A program of five quasi-static tests is conducted in displacement control at a rate of 1 mm/min to establish this property, following the procedure described in Deliverable Report D5-2.

The fatigue testing is then performed under load-control using a sinusoidal waveform defined in Fig. 5-2. The load ratio, R, is set for all tests to a small, fixed value of $R = 0.1$ to ensure that coupons are continuously loaded during testing while still being subjected to a near-complete loading-unloading cycle. In turn, a frequency of $f = 2$ Hz is selected to minimize adverse effects owing to the strain rate dependency of glass fibres and hysteresis heating of viscoelastic polymer matrices above 4 Hz. Similar values have been selected in studies investigating the flexural fatigue of GFRP laminates [46, 47].

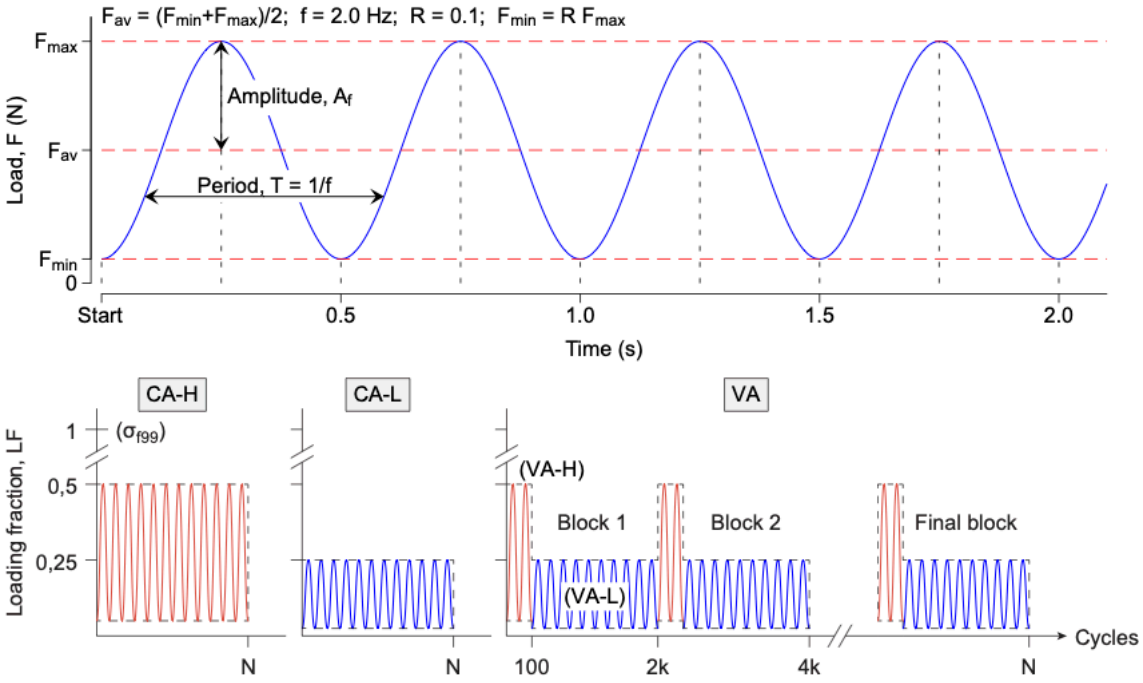

Figure 5-2. Schematics of the sinusoidal waveform and load sequences used in fatigue.

The test procedure is implemented in *Instron's WaveMatrix* dynamic test control software (*version 1.8*). The program filters the machine displacement channel, which corresponds to the roller displacement, to monitor the minimum and maximum peak values per cycle. Peak values are recorded for the machine displacement, load and laser displacement channels at prescribed cycle increments from which the midspan deflection, s, the maximum flexural stress, $\sigma_{f,max}$, and strain, $\varepsilon_{f,max}$, are calculated in accordance with ISO-14125 [45]. Deliverable Report D5-2 provides additional details regarding the general fatigue test procedure.

The fatigue testing program consists of two load amplitudes with $LF = 0.5$ for the high amplitude (CA/VA-H: 50% of $T99$) and to $LF = 0.25$ for the low amplitude (CA/VA-L: 25% of $\mathrm{T99}$). These levels are selected based on exploratory tests and are generally consistent with levels used in the literature such as in [27]. Five coupons are first tested under CA-H loading. Next, five coupons are tested

under VA loading with repeating blocks of 2k cycles consisting of a 1:10 ratio of H- to L-cycles (100:1,9k cycles), the same ratio used in [27]. The use of short H-blocks was first shown in [11, 2] to increase the cycle mixing effect so long as the fatigue life under CA-H loading is a thousand times greater. The test duration for CA-H and VA tests is set to 200k and 500k cycles, respectively, based on exploratory tests, and extended for a number of tests, when the reference damage state has not yet been reached (i.e. intralaminar damage reaching the first and only tensile ply interface between plies 3 and 4). Finally, a single coupon is tested under CA-L loading with a duration of 2 million cycles (~12 days of testing).

5.3. Results and discussion

The transverse flexural stiffness and strength properties of the UD laminate supplied for Task 5-4 are noticeably lower than those of the corresponding laminate supplied for Task 5-2 as shown in Table 5-1. The new A-basis allowable is calculated to be 45.2 MPa, a -22.3% percent difference, owing to a lower mean strength at break and a larger data scatter.

(MPa)	Flexural modulus, E_f [SD]	Strength at break, σ_{fB} [SD]	A-basis allowable, T99
Task 5-2	13 300 [222]	84.2 [5.04]	55.3
Task 5-4	12 700 [306]	77.7 [5.04*]	45.2
Percent difference	-4,72 %	-8,37 %	-22,3 %

*Not a mistake.

Table 5-1. Quasi-static testing results comparing laminates for Task 5-2 and 5-4.

Stress levels are then calculated for H- and L-cycles based $T99$, followed by the respective load levels for each specimen given the selected loading conditions (CA-H, VA or CA-L), given specimen dimensions and set support spans. Figure 5-3 presents the fatigue curves in terms of midspan deflection, s, and apparent stiffness degradation, D, as a function of the number of load cycles. The parameter E_f is simply estimated for each recorded cycles as the ratio of $\sigma_{f,max}$ and $\varepsilon_{f,max}$. As such, E_f is an apparent measure of the flexural stiffness in the coupon midspan. The stiffness degradation, D, is then the relative difference of the current and initial stiffness, $E_{f,i}$ and $E_{f,0}$, respectively.

Both the deflection and stiffness degradation curves are characterized by a general S-shape with notable lumpiness. It is therefore necessary to physically inspect every coupon during testing to properly relate a given transition in damage rate to a specific event, in this case, the presence of clear matrix cracking having reached the first tensile ply interface between plies 3 and 4 (Figure 5-4). The translucent nature of GFRP laminates and the clear effect of the NCF reinforcement architecture, rendered the observation of intralaminar damage readily visible to the naked eye between fibre bundles. This transition typically occurred before a 10% reduction in apparent stiffness, which indicates that ply 4 is still load-bearing at this stage. A stiffness reduction of at least 42% can be expected to ensue based on a quarter reduction in beam thickness alone. Finally, the cycle number corresponding to the transition is obtained via a bilinear regression of the local data points. As shown in Figure 5-3, it takes on average 60% fewer H-cycles under VA loading for intralaminar damage to reach the tensile ply interface than it does under CA-H loading (21,2k compared to 52,7k cycles, respectively). The large scatter data scatter is primarily due to the NCF architecture and the presence of distinct fibre bundles and intralaminar resin-rich pockets, as described in Deliverable Report D5.2. Coupon placement may also play a significant role in accelerating damage initiation due to the proximity of intralaminar (inter-bundle) resin pockets, where cracking is known to initiate, to the sharp stress concentration under the central rollers.

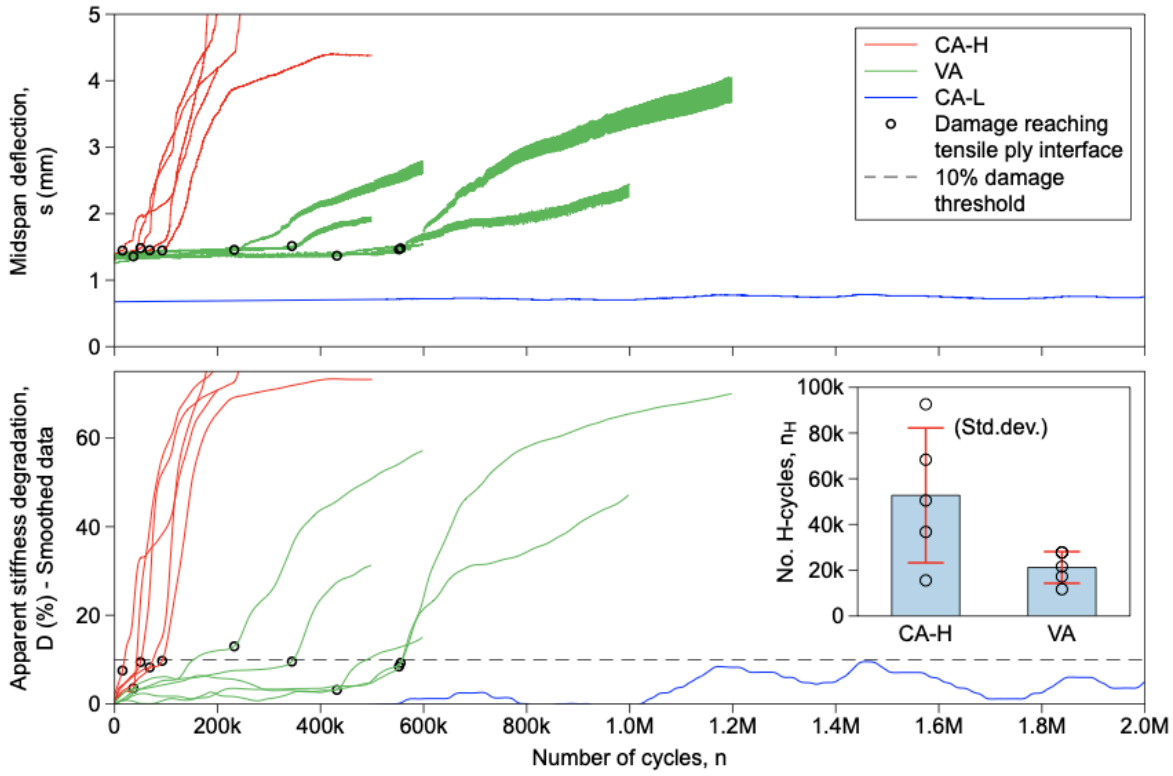

Figure 5-3. Plot of the midspan deflection and apparent stiffness degradation curves.

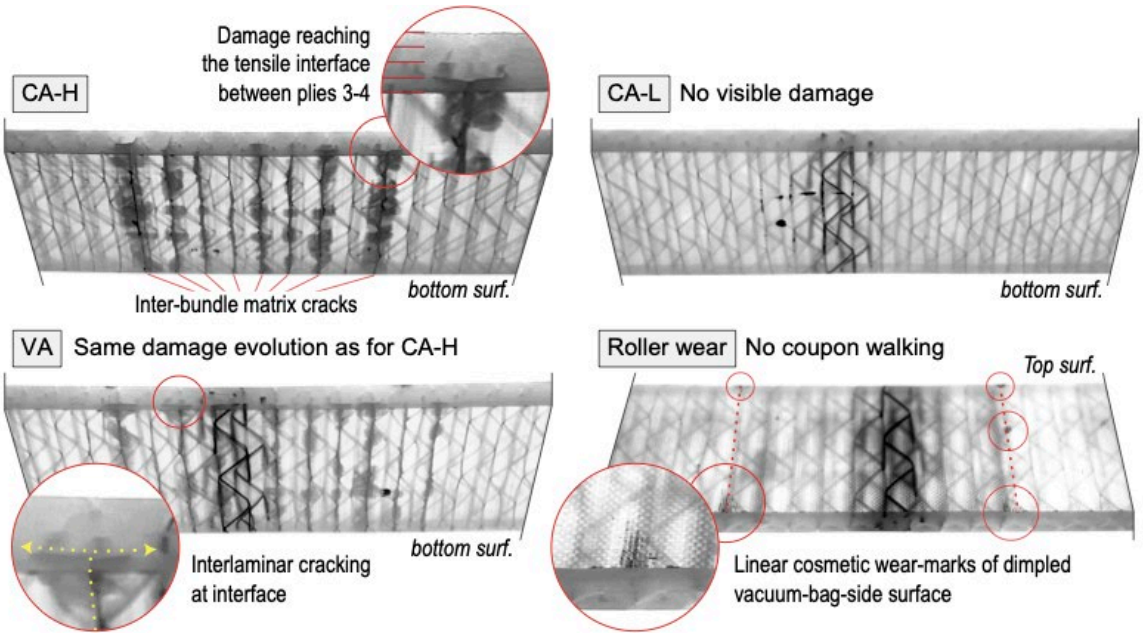

Figure 5-4. Photographic evidence of the typical observed damage for each load case.

Meanwhile, no damage was observed during or after the single CA-L test (Figure 5-4). Time allowing, both the test duration and number of specimens would have been extended. For the purposes of this work, the single test can serve as anecdotal evidence that L-blocks likely contribute very little in the way of intralaminar damage initiation under VA loading, as was concluded by in [27]. As an aside, the apparent stiffness degradation curves for the VA and notably CA-L load cases are unexpectedly rough. Reliance on apparent stiffness is likely to blame. Any systematic error stemming from the test equipment has been ruled out. The assumptions of simple beam theory when calculating the maximum stress and strain simply do not hold. The coupon midspan is subjected a highly localized, non-uniform and progressive damage state. The reason for calculating the apparent stiffness is to

directly compare coupons tested under different load amplitudes. However, the deflection data when paired with visual inspection proved sufficient to capture noteworthy changes in stiffness and to match them to a visible damage state common across load-cases.

6. Conclusion

Task 5.4 firstly focuses on load interaction effects in fatigue-driven delamination. A new phenomenon in the crack growth rate under VA loading called transient delamination growth, which is a transient phase with a significantly increased crack growth rate that follows load amplitude changes in VA load spectra, has recently been observed and characterised [29, 31]. In this work AAU has conducted an experimental test campaign to further characterise transient phenomena in the crack growth rate from two-level block loading tests. The findings are used to propose a new crack growth rate model for prediction of delamination growth under multi-level block loading. The new model evaluates the current crack growth rate from two sources: A steady-state non-interaction term, which is characterised from constant amplitude loading tests, and a transient interaction term, which is characterised from two-level block loading tests. The transient term introduces load history effects in the crack growth rate model. AAU conducted multi-level block loading tests to study transient delamination growth phenomena under load spectra with increased complexity and to evaluate the performance of the new crack growth rate model. AAU has developed a new test setup, which uses the pure moment loaded double cantilever beam specimen in mode I crack opening. The test setup enables cyclic crack growth with real-time control of the applied energy release rate, ERR. The experimental results on two-level block loading confirm that transient crack growth phenomena are significant. The transient crack growth rate following the load amplitude changes are well-described by exponential decay functions, whose parameters have been correlated to governing fatigue load parameters that describe the load history. Analyses of the crack growth rate during multi-level block loading tests prove that many of the transient phenomena observed in the two-level block loading tests also apply when the delamination propagates under more complex VA load spectra. The new crack growth rate model reduces the error in delamination growth predictions in comparison to conventional non-interaction crack growth rate models. The new model represents the crack growth rate following HL load amplitude changes of the multi-level block loading test very well. However, the predictive capability of the new crack growth rate function depends on the characteristics of the load events in the multi-level block loading spectrum.

The new crack growth rate model has been implemented in a finite element formulation using fatigue cohesive zone models. AAU has extended the inter-laminar fatigue damage finite element method from Task 5.1 and SAMTECH has implemented the method in the Simcenter Samcef software and validated it numerically. The simulated results from the Simcenter Samcef solver show a significant improvement in the crack length prediction in comparison to the conventional non-interaction model prediction.

SINTEF performed a targeted test campaign inspired by the experimental work in [27] on intralaminar crack initiation and propagation during VA block loading, while devising a simpler test configuration and damage state monitoring method that can be readily implemented by most any research group with access to a universal fatigue testing machine. The simplified experimental setup used in this work was suitable to investigate the load history effects on intralaminar damage evolution in a GFRP laminate relevant for current wind-turbine production. The reliance on deflection monitoring alone to estimate damage accumulation was sufficient for the observation of noteworthy damage events in tandem with physical observation of coupons during testing. The point at which intralaminar damage (i.e. inter-bundle matrix cracking) reaches the first tensile ply interface was selected as a common damage event across load cases. This reference event allowed for the comparison H-cycle contributions per load case, finding that it takes on average 60% fewer cycles to reach this state under VA loading than it does under CA-H loading. Limited evidence further suggests a negligible contribution from L-cycles, though additional CA-L tests should be carried out over a longer duration. This activity was limited by the scope of Task 5-4 regarding intralaminar testing.

In terms of model applicability, Task 5-2 centred on the implementation of Van Paepegem's intralaminar fatigue damage model [48] in an industrial FE-code, accompanied by an experiment-based, inverse parameter estimation (Deliverable Report D5.2). The same flexural test setup and

approach was used in the present work. This model importantly assumes the stiffness evolution to be independent of load history [44] similar to previous approaches [34]. The modelling approach therefore needs to be further developed in order to capture the significance of the load history effect, as measured herein. Two complications must also be addressed. First, the trained model performed reasonably well for CA-H loading over stages I and II of the damage progression but was notably unable to accurately predict failure during stage III. The GFRP laminate used in this project consists of a NCF reinforcement architecture, resulting in a complex meso-structure and the onset of non-intralaminar damage early in the fatigue life. Second, flexural stiffness is estimated using an idealized FE-model in a manner similar to the apparent stiffness herein, which does not take into consideration the highly localized and complex damage state in the coupon midspan.

7. Bibliography

[1] P. Heuler and H. Klätschke, “Generation and use of standardised load spectra and load-time histories,” *International Journal of Fatigue,* vol. 27, pp. 974-990, 2005.

[2] I. Farrow, “Damage accumulation and degradation of composite laminates under aircraft service loading: Assessment and prediction volume I and II,” PhD thesis, Cranfield Institute of Technology, 1998.

[3] N. Post, S. Case and J. Lesko, “Modeling the variable amplitude fatigue of composite materials: A review and evaluation of state of the art for spectrum loading,” *International Journal of Fatigue,* vol. 30, pp. 2064-2086, 2008.

[4] J. Bartley-Cho, S. Lim, H. Hahn and P. Shyprykevich, “Damage accumulation in quasi-isotropic graphite/epoxy laminates under constant-amplitude fatigue and block loading,” *Composites Sci. Technol.,* vol. 58, pp. 1535-1547, 1998.

[5] E. Gamstedt and B. Sjögren, “On the sequence effect in block amplitude loading of cross-ply composite laminates,” in *Proc. Second Int. Conf. on Fatigue of Composites*, Williamsburg, VA, 2000.

[6] L. Broutman and S. Sahu, “A new theory to predict cumulative fatigue damage in fiberglass reinforced plastics,” in *ASTM STP 497 American Society for Testing and Materials*, Philadelphia, 1972.

[7] H. Whitworth, “Cumulative damage in composites,” *J. Eng. Mater. Technol.,* vol. 112, pp. 358-361, 1990.

[8] R. Sarfaraz, A. Vassilopoulos and T. Keller, “Block loading fatigue of adhesively bonded pultruded GFRP joints,” *International Journal of Fatigue,* vol. 49, pp. 40-49, 2013.

[9] W. Hwang and K. Han, “Cumulative Damage models and Multi-Stress Fatigue Life Prediction,” *Journal of Composite Materials,* vol. 20, pp. 125-153, 1986.

[10] W. Paepegem and J. Degrieck, “Effects of Load Sequence and Block Loading on the Fatigue Response of Fiber-Reinforced Composites,” *Mechanics of Advanced Materials and Structures,* vol. 9, pp. 19-35, 2002.

[11] J. Schaff and B. Davidson, “Life Prediction Methodology for Composite Structures. Part I - Constant Amplitude and Two-Stress Level Fatigue,” *Journal of Composite Materials,* vol. 31, no. 2, pp. 128-157, 1997.

[12] J. Schaff and B. Davidson, “Life Prediction Methodology for Composite Structures. Part II - Spectrum Fatigue,” *Journal of Composite Materials,* vol. 31, no. 2, pp. 158-181, 1997.

[13] P. Filis, I. Farrow and I. Bond, “Classical fatigue analysis and load cycle mix-event damage accumulation in fibre reinforced laminates,” *International Journal of Fatigue,* vol. 26, pp. 565-573, 2004.

[14] M. Bourchak, I. Farrow, I. Bond, C. Rowland and F. Menan, “Acoustic emission energy as fatigue damage parameter for CFRP composites,” *International Journal of Fatigue,* vol. 29, pp. 457-470, 2007.

[15] S. Erpolat, I. Ashcroft, A. Crocombe and M. Abdel-Wahab, “A study of adhesively bonded joints subjected to constant and variable amplitude fatigue,” *International Journal of Fatigue,* vol. 26, pp. 1189-1196, 2004.

[16] V. Passipoularidis, T. Philippidis and P. Brondsted, “Fatigue life prediction in composites using progressive damage modelling under block and spectrum loading,” *International journal of fatigue,* vol. 33, pp. 132-144, 2011.

[17] I. Bond, “Fatigue life prediction for GRP subjected to variable amplitude loading,” *Composites: Part A,* vol. 30, pp. 961-970, 1999.

[18] I. Bond and I. Farrow, “Fatigue life prediction under complex loading for XAS/914 CFRP incorporating a mechanical fastener,” *International Journal of Fatigue ,* vol. 22, pp. 633-644, 2000.

[19] R. Sarfaraz, A. Vassilopoulos and T. Keller, “Variable amplitude fatigue of adhesively-bonded pultruded GFRP joints,” *International Journal of Fatigue,* vol. 55, pp. 22-32, 2013.

[20] A. Poursartip and P. Beaumont, “The Fatigue Damage Mechanics of a Carbon Fibre Composite Laminate: II - Life Prediction,” *Composites Science and Technology,* vol. 25, pp. 283 - 299, 1986.

[21] D. Schütz, H. Lowak, J. de Jonge and J. Schijve, “A standardised load sequence for flight simulation tests on transport aircraft wing structures,” *LBF-Report FB-106, NLR-Report TR 73,* 1973.

[22] W. Aicher, J. Branger, G. van Dijk, J. Ertelt, M. Hück, J. de Jonge and e. al., “Description of a fighter aircraft loading standard for fatigue evaluation FALSTAFF,” *Common report of F+W Emmen, LBF, NRL, IABG,* 1976.

[23] A. ten Have, “WISPER and WISPERX - final definition of two standardised fatigue loading sequences for wind turbine blades,” *NLR Report CR 91476 L, Amsterdam,* 1991.

[24] T. Philippidis and A. Vassilopoulos, “Life prediction methodology for GFRP laminates under spectrum loading,” *Composites part A,* vol. 35, pp. 657-666, 2004.

[25] N. Himmel, “Fatigue life prediction of laminated polymer matrix composites,” *International Journal of Fatigue,* vol. 24, pp. 349-360, 2002.

[26] N. Post, J. Cain, K. McDonald, S. Case and J. Lesko, “Residual strength prediction of composite materials: Random spectrum loading,” *Engineering Fracture Mechanics,* vol. 75, pp. 2707-2724, 2008.

[27] J. Bender, B. Bak, S. Jensen and E. Lindgaard, “Effect of variable amplitude block loading on intralaminar crack initiation and propagation in multidirectional GFRP laminate,” *Composites Part B,* vol. 217, p. 108905, 2021.

[28] S. Erpolat, I. Ashcroft, A. Crocombe and M. Abdel-Wahab, “Fatigue crack growth acceleration due to intermittent overstressing in adhsievely bonded CFRP joints,” *Composites: Part A,* vol. 35, pp. 1175-1183, 2004.

[29] S. Jensen, B. Bak, J. Bender, L. Carreras and E. Lindgaard, “Transient delamination growth in GFRP laminates with fiber bridging under variable amplitude loading in G-control,” *Composites Part B: Engineering,* vol. 225, p. 109296, 2021.

[30] L. Yao, R. Alderliesten and R. Benedictus, “Fatigue delamination growth behaviour in composite materials under block loading,” in *Proceedings of the American Society for Composites - 31st Technical conference*, SAC 2016, 2016.

[31] S. Jensen, B. Bak, J. Bender and E. Lindgaard, “Transition-behaviours in fatigue-driven delamination of GFRP laminates following step changes in block amplitude loading,” *International Journal of Fatigue,* vol. 144, p. 106045, 2021.

[32] J. Glud, J. Dulieu-Barton, O. Thomsen and L. Overgaard, “Automated counting of off-axis tunelling cracks using digital image processing,” *Composites Science and Technology,* vol. 125, pp. 80-89, 2016.

[33] B. Bak, C. Sarrado, A. Turon and J. Costa, “Delamination under fatigue loads in composite laminates: A review on the observed phenomenology and computational methods,” *Applied Mechanics Reviews,* vol. 66, no. 6, p. 060803 (24 pages), 2014.

[34] J. Degrieck and W. Van Paepegem, “Fatigue Damage Modelling of Fibre-reinforced Composite Materials: Review,” *Applied Mechanics Reviews,* vol. 54, no. 4, pp. 279-300, 2001.

[35] L. Carreras, A. Turon, B. Bak, E. Lindgaard, J. Renart, F. Martin de la Escalera and Y. Essa, “A simulation method for fatigue-driven delamination in layered structures involving non-negligible fracture process zones and arbitrarily shaped crack fronts,” *Composites Part A,* vol. 122, pp. 107-119, 2019.

[36] J. Dessureault and J. Spelt, “Observations fo fatigue crack initiation and propagation in an epoxy adhesive,” *Int. J. Adhesion and Adhesives,* vol. 17, pp. 183-195, 1997.

[37] B. Bak and E. Lindgaard, “A method for automated digital image-based tracking of delamination fronts in translucent glass fibre-laminated composite materials,” *Strain,* vol. 56, p. e12345, 2020.

[38] B. Sørensen, “Delamination fractures in composite materials,” in *Modeling Damage, Fatigue and Failure of Composite Materials*, A. Talreja and J. Varna, Eds., , Woodhead Publishing Series in Composites Science and Engineering: Number 65, 2016, p. Chapt. 11.

[39] S. Winitzki, “Uniform approximations for transcedental functions,” in *International Conference on Computational Science and Its Applications*, Berlin, Heidelberg, 2003, May.

[40] H. Shen, W. Yao, W. Qi and J. Zong, “Experimental investigation on damage evolution in cross-ply laminates subjected to quasi-static and fatigue loading,” *Composites Part B: Engineering,* vol. 120, pp. 10-26, 2017.

[41] J. Glud, J. Dulieu-Barton, O. Thomse and L. Overgaard, “Fatigue damage evolution in GFRP laminates with constrained off-axis plies,” *Composites: Part A,* vol. 95, pp. 359-369, 2017.

[42] M. Quaresimin, P. Carraro, L. Mikkelsen, N. Lucato, L. Vivian, P. S. B. Brønsted, J. Varna and R. Talreja, “Damage evolution under cyclic multiaxial stress state: A comparative analysis between glass/epoxy laminates and tubes,” *Composites Part B: Engineering,* vol. 61, pp. 282-290, 2014.

[43] K. Ogi, S. Yashiro and K. Niimi, “A probabilistic approach for transverse crack evolution in a composite laminate under variable amplitude cyclic loading,” *Composites Part A: Applied Science and Manufacturing,* vol. 41, no. 3, pp. 383-390, 2010.

[44] D. e. a.-. Carrella-Payan, “Implementation of fatigue model for unidirectional laminate based on finite element analysis: Theory and practice,” *Frattura ed Integritá Strutturale,* vol. 10, no. 38, pp. 184-190, 2016.

[45] I. standardization, “Fibre-reinforced plastic composites - Determination of flexural properties,” *International Organization for Standardization: Geneva, Switzerland,* p. p. 18, 2004.

[46] W. Van Paepegem and J. Degrieck, “Experimental set-up for a numerical modelling of bending fatigue experiments on plain woven glass/epoxy composites,” *Composite Structures,* vol. 51, no. 1, pp. 1-8, 2001.

[47] W. Van Paepegem and J. Degrieck, “A new coupled approach of residual stiffness and strength for fatigue of fibre-reinforced composites,” *International Journal of Fatigue,* vol. 24, no. 7, pp. 747-762, 2002.

[48] W. Van Paepegem, “Development and finite element implementation of a damage model for fatigue of fibre-reinforced polymers,” *Ghent, Belgium: Ghent University Architectural and Engineering Press,* 2002.

[49] H. Z, “Cumulative Damage Theory for Composite Materials: Residual life and Residual Strength Methods,” *Composites Science and Technology,* vol. 23, pp. 1-19, 1985.

[50] J. Yang and D. Jones, “Effect of load sequence on the statistical fatigue of composites,” *AIAA journal,* vol. 18, no. 12, pp. 1525-1531, 1980.

[51] A. Plumtree, M. Melo and J. Dahl, “Damage evolution in a [+/-45] 2S CFRP laminate under block loading conditions,” *International Journal fo Fatigue,* vol. 32, no. 1, pp. 139-145, 2010.